International Journal of Plasticity 109 (2018) 193–211

Contents lists available at ScienceDirect

International Journal of Plasticity

journal homepage: www.elsevier.com/locate/ijplas

Modeling of intragranular misorientation and grain fragmentation in polycrystalline materials using the viscoplastic self-consistent formulation

Miroslav Zecevic[a], Ricardo A. Lebensohn[b], Rodney J. McCabe[b], Marko Knezevic[a,*]

[a] Department of Mechanical Engineering, University of New Hampshire, Durham, NH 03824, United States
[b] Materials Science and Technology Division, Los Alamos National Laboratory, Los Alamos, NM 87544, United States

ARTICLE INFO

Keywords:
Microstructures
Crystal plasticity
Viscoplastic material
Numerical algorithms
GF-VPSC

ABSTRACT

The recently established methodology to use known algorithmic expressions of the second moments of the stress field in the grains of a polycrystalline aggregate for calculating average fluctuations of lattice rotation rates and the associated average intragranular misorientation distributions using the mean-field viscoplastic self-consistent (VPSC) formulation is extended to solve the coupled problem of considering the effect of intragranular misorientations on stress and rotation rate fluctuations. In turn, these coupled expressions are used to formulate and implement a grain fragmentation (GF) model in VPSC. Case studies, including tension and plane-strain compression of face-centered cubic polycrystals are used to illustrate the capabilities of the new model. GF-VPSC predictions of intragranular misorientation distributions and texture evolution are compared with experiments and full-field numerical simulations, showing good agreement. In particular, the inclusion of misorientation spreads reduced the intensity of the deformed texture and thus improved the texture predictions. Moreover, considering that intragranular misorientations act as driving forces for recrystallization, the new GF-VPSC formulation is shown to enable modeling of microstructure evolution during deformation and recrystallization, in a computationally efficient manner.

1. Introduction

Mean-field polycrystal plasticity models provide a balance between computational efficiency and accuracy. One of such models is the widely-used viscoplastic self-consistent (VPSC) formulation (Lebensohn and Tomé, 1993). In VPSC, each single crystal grain is represented as an ellipsoidal inclusion within a matrix that has the averaged properties of all grains. The state of each inclusion/grain is described by the average values of the micromechanical (stress and strain rate), and microstructural (slip resistance and orientation) fields inside the grain, which evolve during deformation. Consequently, the effect of intragranular misorientation developing in the grains as deformation accumulates is not accounted for (Winther et al., 2017).

Accurate predictions of the intragranular misorientation distributions at high strains are important for simulation of deformation textures and necessary for modeling of recrystallization. Mean-field models tend to predict sharper deformation textures than experimental measurements and those predicted by full-field models, because the orientation distribution of each grain is described only by one mean orientation (Jahedi et al., 2018; Knezevic et al., 2008, 2012; Lebensohn, 2001). Therefore, incorporation and

* Corresponding author. University of New Hampshire, Department of Mechanical Engineering, 33 Academic Way, Kingsbury Hall, W119, Durham, NH 03824, United States.
E-mail address: marko.knezevic@unh.edu (M. Knezevic).

https://doi.org/10.1016/j.ijplas.2018.06.004
Received 22 February 2018; Received in revised form 31 May 2018; Accepted 8 June 2018
Available online 15 June 2018
0749-6419/

consideration of intragranular misorientation spreads in mean-field models can improve texture predictions, reducing peak intensities in orientation space. Moreover, modeling of recrystallization of deformed polycrystals also requires accurate predictions of intragranular misorientations. Misorientation distributions can be used as indicators of whether a given grain has developed deformation and transition bands, and the trends of the crystal orientations developing within those bands can be identified as well. Transition bands are regions of high orientation gradients between deformation bands and, therefore, are favorable places for nucleation of recrystallization (Dillamore and Katoh, 1974; Humphreys and Hatherly, 2004). Recrystallization nuclei are observed to develop from the subgrains already present in the transition band (Humphreys and Hatherly, 2004; Ridha and Hutchinson, 1982). Hence, prediction of transition bands and the crystallographic orientations present in them is crucial for the prediction of recrystallization textures.

In the last decade, the VPSC formulation was extended to calculate intragranular second moments of stress, which statistically describe the stress fields inside the grains, beyond their average values (Lebensohn et al., 2004, 2007). These second moments can be used to obtain a better linear approximation of the grain's non-linear constitutive behavior (Castañeda, 2002; Doghri et al., 2011; Liu and Castañeda, 2004). In our recent work, we have utilized these second moments of stress to obtain average fluctuations of the lattice rotation rate field in each grain (Lebensohn et al., 2016). Moreover, a time integration procedure of the latter for updating the average intragranular misorientations was developed in (Zecevic et al., 2017), and used for the prediction of intragranular misorientation spreads at moderate strains.

In order to accurately predict the intragranular misorientation spreads at higher strains, the current model must be improved to include grain fragmentation and the mutual influence of intragranular misorientations, and stress and rotation rate fluctuations. The intragranular orientation distribution may become quite large at higher strains (Jahedi et al., 2015, 2017; Liu et al., 1998) and thus it cannot be represented accurately with only one mean value and one second moment (Ardeljan et al., 2015, 2016; Buchheit et al., 2015; Kanjarla et al., 2010; Quey et al., 2012). Therefore, a grain fragmentation criterion becomes necessary at those high strains. Several ad-hoc grain fragmentation models have been developed within mean-field frameworks, and were capable of predicting the reduction in grain size and the increase in high-angle boundaries with strain (Beyerlein et al., 2003; Butler and McDowell, 1998; Jahedi et al., 2014; Kumar and Mahesh, 2013; Lee and Duggan, 1993; Ostapovets et al., 2012; Tomé et al., 2002; Toth et al., 2010). However, none of these approaches utilize the micromechanically consistent intragranular stress fluctuations as the driving force for the fragmentation. It is important to note that VPSC provides only a statistical description (i.e. average) of fluctuations within the grains. Hence, the actual spatial distribution of the fluctuations within the grains remains unknown. Consequently, the approach cannot *directly* predict the increase in high-angle boundaries, reduction of grain size and formation of intragranular orientation gradients. However, additional assumptions describing the spatial correlation of the intragranular misorientation spread can be introduced. Moreover, cumulative misorientation within grains causes additional fluctuations of stress and lattice rotation rates, and these become significant as the magnitude of misorientation spread increases. These corrections need to be accounted for, since they are essential for predicting the development of intragranular fluctuations at higher strains.

In this paper, the standard VPSC model is extended to calculate intragranular misorientation distributions at high strains. First, the second moments of intragranular stresses calculated with VPSC (Lebensohn et al., 2004, 2007) are extended to include the influence of the intragranular misorientations. Next, the second moments of lattice rotation rate calculated based on the second moment of stress (Lebensohn et al., 2016), are also extended to include the influence of the intragranular misorientation. The second moments of lattice rotation rate are then accounted for in the calculation of intragranular misorientation spreads (Zecevic et al., 2017). These improvements allow more accurate predictions of intragranular misorientations developing at high strains. Finally, a grain fragmentation (GF) model is formulated in orientation space. This GF-VPSC model is applied to simulate tension and plane-strain compression (PSC) of face-centered cubic (fcc) polycrystals. The predicted intragranular misorientation distributions and texture evolution are compared with experimental data taken from (Quey et al., 2010) for rolled Al, and full-field calculations obtained using the viscoplastic Fast Fourier Transform-based (VPFFT) micromechanical model (Lebensohn, 2001; Lebensohn et al., 2008). Additionally, the GF-VPSC model is shown to enable modeling of evolution of microstructural features necessary for subsequent recrystallization modeling in a computationally efficient manner.

2. Modeling framework

This section summarizes the standard VPSC formulation (Lebensohn and Tomé, 1993) and then describes the algorithms to calculate intragranular stress and lattice rotation rate fluctuations, and intragranular misorientation distributions (Lebensohn et al., 2004, 2016; Zecevic et al., 2017). These developments are combined in the new grain fragmentation model implemented in VPSC, which is termed GF-VPSC.

In the adopted notation, the inner products between two vectors or tensors are denoted by "." (summation over one contracted index), ":" (summation over two contracted indices) and "::" (summation over four contracted indices). The outer product of two tensors is denoted by "⊗".

2.1. Standard VPSC formulation

The viscoplastic strain rate, $\dot{\boldsymbol{\varepsilon}}(\mathbf{x})$, at single crystal material point $\mathbf{x}$ deforming by dislocation glide is given by:

$$\dot{\boldsymbol{\varepsilon}}(\mathbf{x}) = \sum_{s} \dot{\gamma}^{s}(\mathbf{x})\mathbf{m}^{s}(\mathbf{x}), \tag{1}$$

where $\mathbf{m}^s(\mathbf{x}) = \frac{1}{2}(\mathbf{b}^s(\mathbf{x}) \otimes \mathbf{n}^s(\mathbf{x}) + \mathbf{n}^s(\mathbf{x}) \otimes \mathbf{b}^s(\mathbf{x}))$ is the symmetric part of the Schmid tensor and $\mathbf{b}^s$ and $\mathbf{n}^s$ are the Burgers vector and slip plane normal of slip system s. $\dot{\gamma}^s(\mathbf{x})$ is the shear rate on slip system s at material point $\mathbf{x}$ given by:

$$\dot{\gamma}^s(\mathbf{x}) = \dot{\gamma}_0 \left(\frac{|\tau^s(\mathbf{x})|}{\tau_c^s(\mathbf{x})} \right)^n \text{sign}(\tau^s(\mathbf{x})), \tag{2}$$

where $\tau^s(\mathbf{x}) = \mathbf{m}^s(\mathbf{x})$: $\boldsymbol{\sigma}(\mathbf{x})$ is the resolved shear stress on slip system s, $\dot{\gamma}_0$ is the reference shear rate, n is the inverse of rate sensitivity, and τ_c^s is the critical resolved shear stress. Substituting Eq. (2) in Eq. (1) gives the non-linear relation (i.e. the *rate-sensitive* constitutive equation) between strain rate and stress:

$$\dot{\boldsymbol{\varepsilon}}(\mathbf{x}) = \dot{\gamma}_0 \sum_s \left(\frac{|\boldsymbol{\sigma}(\mathbf{x}) : \mathbf{m}^s(\mathbf{x})|}{\tau_c^s(\mathbf{x})} \right)^n \text{sign}(\boldsymbol{\sigma}(\mathbf{x}) : \mathbf{m}^s(\mathbf{x}))\mathbf{m}^s(\mathbf{x}). \tag{3}$$

The non-linear relationship at the slip system level (Eq. (2)) can be linearized as:

$$\dot{\gamma}^s(\mathbf{x}) = \eta^{s(r)}\tau^s(\mathbf{x}) + \dot{g}^{0s(r)}, \tag{4}$$

where $\eta^{s(r)}$ and $\dot{g}^{0s(r)}$ are the linearized compliance and the back-extrapolated shear rate of slip system s in grain r. Consequently, the linearized behavior at the grain level is given by:

$$\dot{\boldsymbol{\varepsilon}}(\mathbf{x}) = \mathbf{M}^{(r)} : \boldsymbol{\sigma}(\mathbf{x}) + \dot{\boldsymbol{\varepsilon}}^{0(r)}, \tag{5}$$

where $\mathbf{M}^{(r)}$ and $\dot{\boldsymbol{\varepsilon}}^{0(r)}$ are the linearized compliance and the back-extrapolated strain rate for grain r. The grain moduli are defined by the linearization procedure. In this work, we adopt the affine linearization (Masson et al., 2000).

Since the grain behavior is now approximated by a linear relation, self-consistent homogenization can be performed, resulting in an analogous linear relation at the macroscopic level:

$$\dot{\mathbf{E}} = \overline{\mathbf{M}} : \boldsymbol{\Sigma} + \dot{\mathbf{E}}^0, \tag{6}$$

where $\dot{\mathbf{E}}$ and $\boldsymbol{\Sigma}$ are the macroscopic strain rate and stress; $\overline{\mathbf{M}}$ and $\dot{\mathbf{E}}^0$ are the macroscopic compliance and back-extrapolated strain rate. In the self-consistent scheme, each single crystal grain is assumed to be an ellipsoidal inhomogeneity embedded in an infinite matrix, to which the boundary conditions are applied and whose macroscopic properties need to be determined from weighted averages over the grain's moduli. Consequently, the spatial arrangement of the grains in the polycrystal has no effect on the predictions of the model. The solution for the strain rate and stress in the inhomogeneity representing each grain orientation is obtained by means of the equivalent Eshelby's inclusion approach (Eshelby, 1957).

The interaction equation, relating the deviations in strain rate, $\tilde{\dot{\boldsymbol{\varepsilon}}}^{(r)}$, and in stress, $\tilde{\boldsymbol{\sigma}}^{(r)}$, in the inhomogeneity with respect to the macroscopic values is (Lebensohn and Tomé, 1993):

$$\tilde{\dot{\boldsymbol{\varepsilon}}}^{(r)} = -\widetilde{\mathbf{M}} : \tilde{\boldsymbol{\sigma}}^{(r)}, \tag{7}$$

where the interaction tensor, $\widetilde{\mathbf{M}}$, is calculated as:

$$\widetilde{\mathbf{M}} = (\mathbf{I} - \mathbf{S})^{-1} : \mathbf{S} : \overline{\mathbf{M}}, \tag{8}$$

where $\mathbf{S}$ is the symmetric Eshelby tensor. The macroscopic properties are calculated via the self-consistent equations:

$$\overline{\mathbf{M}} = \langle \mathbf{M}^{(r)} : \mathbf{B}^{(r)} \rangle, \tag{9}$$

$$\dot{\mathbf{E}}^0 = \langle \mathbf{M}^{(r)} : \mathbf{b}^{(r)} + \dot{\boldsymbol{\varepsilon}}^{0(r)} \rangle, \tag{10}$$

where $\mathbf{B}^{(r)}$ and $\mathbf{b}^{(r)}$ are stress localization tensors relating the macroscopic stress and stress in grain r, given by:

$$\mathbf{B}^{(r)} = (\mathbf{M}^{(r)} + \widetilde{\mathbf{M}})^{-1} : (\overline{\mathbf{M}} + \widetilde{\mathbf{M}}), \tag{11}$$

$$\mathbf{b}^{(r)} = (\mathbf{M}^{(r)} + \widetilde{\mathbf{M}})^{-1} : (\dot{\mathbf{E}}^0 - \dot{\boldsymbol{\varepsilon}}^{0(r)}), \tag{12}$$

and where $\langle\rangle$ denotes volume average. The self-consistent equations are implicit in macroscopic moduli, $\overline{\mathbf{M}}$ and $\dot{\mathbf{E}}^0$, and are thus solved numerically using a fix-point method.

In the absence of an applied macroscopic rigid-body rotation, the total lattice rotation rate at a material point $\mathbf{x}$ belonging to grain r is given by:

$$\dot{\boldsymbol{\omega}}(\mathbf{x}) = \widetilde{\dot{\boldsymbol{\omega}}}^{(r)} - \dot{\boldsymbol{\omega}}^p(\mathbf{x}), \tag{13}$$

where $\widetilde{\dot{\boldsymbol{\omega}}}^{(r)} = \boldsymbol{\Pi} : \mathbf{S}^{-1} : \tilde{\dot{\boldsymbol{\varepsilon}}}^{(r)}$ is the rigid-body rotation rate of the ellipsoidal inclusion and $\boldsymbol{\Pi}$ is the anti-symmetric Eshelby tensor. $\dot{\boldsymbol{\omega}}^p(\mathbf{x})$ is the lattice rotation rate at material point $\mathbf{x}$ of grain r calculated as:

$$\dot{\boldsymbol{\omega}}^p(\mathbf{x}) = \sum_s \dot{\gamma}^s(\mathbf{x})\boldsymbol{\alpha}^s(\mathbf{x}), \tag{14}$$

where $\boldsymbol{\alpha}^s(\mathbf{x}) = \frac{1}{2}(\mathbf{b}^s(\mathbf{x}) \otimes \mathbf{n}^s(\mathbf{x}) - \mathbf{n}^s(\mathbf{x}) \otimes \mathbf{b}^s(\mathbf{x}))$ is the antisymmetric part of the Schmid tensor of slip system s.

2.2. Stress fluctuations

After convergence of the self-consistent scheme at time t, the mean values of micromechanical fields in the grains and the effective properties of the polycrystal are known, and the average fluctuations (second moment of the distribution) of the stress field within each grain can be determined, as well (Lebensohn et al., 2007). Since the grain volume average of intragranular fluctuations of any field variable is zero, the fluctuations do not affect the mean values in any way. In what follows, we represent the symmetric deviatoric second-rank tensors as five-dimensional vectors (Lebensohn and Tomé, 1993; Lequeu et al., 1987) and antisymmetric second-rank tensors as three-dimensional dual vectors.

Let us first assume a homogeneous orientation within each grain r, given by the active rotation quaternion at time t, $\overline{\mathbf{q}}^{t(r)}$, which brings the sample frame into alignment with the crystal frame. Spatial variations of mean grain properties from grain to grain cause fluctuations in stress, $\delta\boldsymbol{\sigma}^{t(\overline{q})}(\mathbf{x})$, within each grain (Bobeth and Diener, 1986):

$$\boldsymbol{\sigma}^t(\mathbf{x}) = \boldsymbol{\sigma}^{t(r)} + \delta\boldsymbol{\sigma}^{t(\overline{q})}(\mathbf{x}). \tag{15}$$

The second moment of stress within each grain can be calculated as (Lebensohn et al., 2004):

$$<\boldsymbol{\sigma}^t \otimes \boldsymbol{\sigma}^t>^{(r)} = \boldsymbol{\sigma}^{t(r)} \otimes \boldsymbol{\sigma}^{t(r)} + <\delta\boldsymbol{\sigma}^{t(\overline{q})} \otimes \delta\boldsymbol{\sigma}^{t(\overline{q})}>^{(r)} = \frac{2}{c^{t(r)}}\frac{\partial \widetilde{U}_T^t}{\partial \mathbf{M}^{t(r)}}, \tag{16}$$

where $\widetilde{U}_T^t$ is the effective stress potential given by:

$$\widetilde{U}_T^t = \frac{1}{2}\overline{\mathbf{M}}^t :: (\boldsymbol{\Sigma}^t \otimes \boldsymbol{\Sigma}^t) + \dot{\mathbf{E}}^{0t} : \boldsymbol{\Sigma}^t + \frac{1}{2}\overline{G}^t. \tag{17}$$

$\overline{G}^t$ is the energy under zero applied stress. This second moment of stress statistically describes the average stress fluctuations within the grain in the absence of the intragranular misorientation. Since the effective properties in Eq. (17) are calculated by the self-consistent procedure, the spatial arrangement of grains in the polycrystal has no influence on the effective stress potential and the stress fluctuations.

We now introduce a misorientation quaternion field, $\delta\mathbf{q}^t(\mathbf{x})$, inside of each grain at time t, which is defined with respect to the mean orientation quaternion of the corresponding grain, $\overline{\mathbf{q}}^{t(r)}$ (Pantleon, 2005). The crystal orientation, $\mathbf{q}^t(\mathbf{x})$, at each material point is then obtained composing the mean orientation of the grain containing the point and the misorientation at that point:

$$\mathbf{q}^t(\mathbf{x}) = \delta\mathbf{q}^t(\mathbf{x})\overline{\mathbf{q}}^{t(r)}. \tag{18}$$

Since three independent variables are enough to fully define a misorientation (or an orientation), we describe the misorientation field with the vector part, $\delta\mathbf{r}^t(\mathbf{x})$, of the misorientation quaternion, $\delta\mathbf{q}^t(\mathbf{x})$ (Pantleon, 2005). The volume average of the vector part of the quaternion misorientation field within each grain vanishes, $<\delta\mathbf{r}^t>^{(r)} = 0$, meaning that the misorientation field does not alter the mean grain orientation, $\overline{\mathbf{q}}^{t(r)}$ (Pantleon, 2005). Consequently, the misorientation field will not affect the mean grain properties and thus it will not influence the existing stress fluctuation $\delta\boldsymbol{\sigma}^{t(\overline{q})}(\mathbf{x})$ in any way. However, since the stress is a function of orientation and thus misorientation (Eq. (3)), the misorientation field will cause additional fluctuations of the stress field, $\delta\boldsymbol{\sigma}^{t(\delta r)}(\mathbf{x})$, at each material point, $\mathbf{x}$, which should be superimposed to the existing stress fluctuations:

$$\boldsymbol{\sigma}^t(\mathbf{x}) = \boldsymbol{\sigma}^{t(r)} + \delta\boldsymbol{\sigma}^{t(\overline{q})}(\mathbf{x}) + \delta\boldsymbol{\sigma}^{t(\delta r)}(\mathbf{x}). \tag{19}$$

As was noted before, the fluctuations within the grains will be described by the corresponding second moments. Calculation of the second moment of a nonlinear function requires knowledge of the higher order moments of the corresponding independent variables, which are not available in our approach. In order to work only with second moments, we perform linearization of each function that depends on variables that vary within the grain (Ang and Tang, 1975). To this end, we approximate the fluctuation of stress due to misorientation variation within the grain, $\delta\boldsymbol{\sigma}^{t(\delta r)}$, with a linear relation between stress fluctuation and the misorientation vector by performing a first order Taylor expansion of the nonlinear Eq. (3) around the mean grain values:

$$\delta\boldsymbol{\sigma}^{t(\delta r)}(\mathbf{x}) = \left.\frac{\partial \boldsymbol{\sigma}}{\partial \delta\mathbf{r}}\right|^t_{\boldsymbol{\sigma}^{(r)},\overline{\mathbf{q}}^{(r)}} \delta\mathbf{r}^t(\mathbf{x}), \tag{20}$$

where $\left.\frac{\partial \boldsymbol{\sigma}}{\partial \delta\mathbf{r}}\right|^t_{\boldsymbol{\sigma}^{(r)},\overline{\mathbf{q}}^{(r)}}$ represents rate of change of stress with misorientation, with the strain rate held constant at the mean grain value, and is given in Appendix A. The fluctuations of stress due to misorientation are hence assumed to be linearly proportional to the misorientation vectors, where the linear map is defined by the derivative of stress with respect to misorientation vector. Eq. (19) implies that there are two fundamental sources of stress fluctuations within each grain: the spatial variation of grain properties within the polycrystal, and the intragranular misorientation field.

Upon consideration of the intragranular misorientations, the second moment of stress in grain r (i.e. Eq. (16)) becomes:

$$<\boldsymbol{\sigma}^t \otimes \boldsymbol{\sigma}^t>^{(r)} = \boldsymbol{\sigma}^{t(r)} \otimes \boldsymbol{\sigma}^{t(r)} + <\delta\boldsymbol{\sigma}^{t(\overline{q})} \otimes \delta\boldsymbol{\sigma}^{t(\overline{q})}>^{(r)} + <\delta\boldsymbol{\sigma}^{t(\delta r)} \otimes \delta\boldsymbol{\sigma}^{t(\delta r)}>^{(r)} + <\delta\boldsymbol{\sigma}^{t(\overline{q})} \otimes \delta\boldsymbol{\sigma}^{t(\delta r)}>^{(r)} + <\delta\boldsymbol{\sigma}^{t(\delta r)} \otimes \delta\boldsymbol{\sigma}^{t(\overline{q})}>^{(r)}. \tag{21}$$

The term $<\delta\boldsymbol{\sigma}^{t(\delta r)} \otimes \delta\boldsymbol{\sigma}^{t(\delta r)}>^{(r)}$ represents the second moment of stress fluctuations caused solely by the misorientation field within the grain, and is given by:

$$<\delta\boldsymbol{\sigma}^{t(\delta r)} \otimes \delta\boldsymbol{\sigma}^{t(\delta r)}>^{(r)} = \frac{\partial\boldsymbol{\sigma}}{\partial\delta\mathbf{r}}\Big|^{t}_{\sigma^{(r)},\bar{\mathbf{q}}^{(r)}} <\delta\mathbf{r}^{t} \otimes \delta\mathbf{r}^{t}>^{(r)} \left(\frac{\partial\boldsymbol{\sigma}}{\partial\delta\mathbf{r}}\Big|^{t}_{\sigma^{(r)},\bar{\mathbf{q}}^{(r)}}\right)^{T}. \tag{22}$$

where $<\delta\mathbf{r}^{t} \otimes \delta\mathbf{r}^{t}>^{(r)}$ represents the second moment of the vector part of the misorientation quaternions in grain r. The last two terms of Eq. (21) are transposed relative to each other and represent the cross-covariance between two stress fluctuations caused by different sources, and are calculated as:

$$<\delta\boldsymbol{\sigma}^{t(\bar{q})} \otimes \delta\boldsymbol{\sigma}^{t(\delta r)}>^{(r)} = <\delta\boldsymbol{\sigma}^{t(\bar{q})} \otimes \delta\mathbf{r}^{t}>^{(r)} \left(\frac{\partial\boldsymbol{\sigma}}{\partial\delta\mathbf{r}}\Big|^{t}_{\sigma^{(r)},\bar{\mathbf{q}}^{(r)}}\right)^{T}, \tag{23}$$

where $<\delta\boldsymbol{\sigma}^{t(\bar{q})} \otimes \delta\mathbf{r}^{t}>^{(r)}$ represents the cross-covariance between the stress fluctuation caused by variation of the mean grain properties in the polycrystal, and the misorientation. The approach for calculation of cross-covariance $<\delta\boldsymbol{\sigma}^{t(\bar{q})} \otimes \delta\mathbf{r}^{t}>^{(r)}$ will be given at the end of this section.

2.3. Lattice rotation rate fluctuations

Once the stress fluctuations have been defined and characterized with second moments, the lattice rotation rate (or *lattice spin*) fluctuations at time t can be calculated as follows. Eqs. (13) and (14) define lattice rotation rate as a nonlinear function of stress and orientation. In order to derive the second moment of the lattice spin as a function of the first and second moments of stress and misorientation, we approximate the fluctuation of the lattice spin within grain r with a first order Taylor expansion around the mean grain value with respect to stress and the vector part of the misorientation quaternion:

$$\dot{\boldsymbol{\omega}}^{t}(\mathbf{x}) = \dot{\boldsymbol{\omega}}^{t(r)} + \frac{\partial\dot{\boldsymbol{\omega}}}{\partial\boldsymbol{\sigma}}\Big|^{t}_{\sigma^{(r)},\bar{\mathbf{q}}^{(r)}} \delta\boldsymbol{\sigma}^{t}(\mathbf{x}) + \frac{\partial\dot{\boldsymbol{\omega}}}{\partial\delta\mathbf{r}}\Big|^{t}_{\sigma^{(r)},\bar{\mathbf{q}}^{(r)}} \delta\mathbf{r}^{t}(\mathbf{x}), \tag{24}$$

where $\frac{\partial\dot{\boldsymbol{\omega}}}{\partial\boldsymbol{\sigma}}\Big|^{t}_{\sigma^{(r)},\bar{\mathbf{q}}^{(r)}}$ and $\frac{\partial\dot{\boldsymbol{\omega}}}{\partial\delta\mathbf{r}}\Big|^{t}_{\sigma^{(r)},\bar{\mathbf{q}}^{(r)}}$ are derivatives of the lattice spin with respect to stress and the vector part of the misorientation quaternion given in Appendix A. Eq. (24) can be rewritten as:

$$\dot{\boldsymbol{\omega}}^{t}(\mathbf{x}) = \dot{\boldsymbol{\omega}}^{t(r)} + \delta\dot{\boldsymbol{\omega}}^{t(\delta\sigma)}(\mathbf{x}) + \delta\dot{\boldsymbol{\omega}}^{t(\delta r)}(\mathbf{x}), \tag{25}$$

where $\delta\dot{\boldsymbol{\omega}}^{t(\delta\sigma)}(\mathbf{x}) = \frac{\partial\dot{\boldsymbol{\omega}}}{\partial\boldsymbol{\sigma}}\Big|^{t}_{\sigma^{(r)},\bar{\mathbf{q}}^{(r)}} \delta\boldsymbol{\sigma}^{t}(\mathbf{x})$ is the lattice spin fluctuation caused by the stress fluctuation (Lebensohn et al., 2016) and $\delta\dot{\boldsymbol{\omega}}^{t(\delta r)}(\mathbf{x}) = \frac{\partial\dot{\boldsymbol{\omega}}}{\partial\delta\mathbf{r}}\Big|^{t}_{\sigma^{(r)},\bar{\mathbf{q}}^{(r)}} \delta\mathbf{r}^{t}(\mathbf{x})$ is the lattice spin fluctuation caused by the misorientation fluctuation. Note that the stress fluctuation, $\delta\boldsymbol{\sigma}^{t}(\mathbf{x})$, contains the effect of the misorientation fluctuation and thus the term $\delta\dot{\boldsymbol{\omega}}^{t(\delta\sigma)}(\mathbf{x})$ also includes the effects of the misorientation fluctuation through the stress.

The second moment of lattice spin is calculated as:

$$\begin{aligned}<\dot{\boldsymbol{\omega}}^{t} \otimes \dot{\boldsymbol{\omega}}^{t}>^{(r)} = {}& \dot{\boldsymbol{\omega}}^{t(r)} \otimes \dot{\boldsymbol{\omega}}^{t(r)} + <\delta\dot{\boldsymbol{\omega}}^{t(\delta\sigma)} \otimes \delta\dot{\boldsymbol{\omega}}^{t(\delta\sigma)}>^{(r)} + <\delta\dot{\boldsymbol{\omega}}^{t(\delta r)} \otimes \delta\dot{\boldsymbol{\omega}}^{t(\delta r)}>^{(r)} + <\delta\dot{\boldsymbol{\omega}}^{t(\delta\sigma)} \otimes \delta\dot{\boldsymbol{\omega}}^{t(\delta r)}>^{(r)} \\ & + <\delta\dot{\boldsymbol{\omega}}^{t(\delta r)} \otimes \delta\dot{\boldsymbol{\omega}}^{t(\delta\sigma)}>^{(r)}.\end{aligned} \tag{26}$$

Expressions for terms on the right hand side are:

$$<\delta\dot{\boldsymbol{\omega}}^{t(\delta\sigma)} \otimes \delta\dot{\boldsymbol{\omega}}^{t(\delta\sigma)}>^{(r)} = \frac{\partial\dot{\boldsymbol{\omega}}}{\partial\boldsymbol{\sigma}}\Big|^{t}_{\sigma^{(r)},\bar{\mathbf{q}}^{(r)}} <\delta\boldsymbol{\sigma}^{t} \otimes \delta\boldsymbol{\sigma}^{t}>^{(r)} \left(\frac{\partial\dot{\boldsymbol{\omega}}}{\partial\boldsymbol{\sigma}}\Big|^{t}_{\sigma^{(r)},\bar{\mathbf{q}}^{(r)}}\right)^{T} \tag{27}$$

$$<\delta\dot{\boldsymbol{\omega}}^{t(\delta r)} \otimes \delta\dot{\boldsymbol{\omega}}^{t(\delta r)}>^{(r)} = \frac{\partial\dot{\boldsymbol{\omega}}}{\partial\delta\mathbf{r}}\Big|^{t}_{\sigma^{(r)},\bar{\mathbf{q}}^{(r)}} <\delta\mathbf{r}^{t} \otimes \delta\mathbf{r}^{t}>^{(r)} \left(\frac{\partial\dot{\boldsymbol{\omega}}}{\partial\delta\mathbf{r}}\Big|^{t}_{\sigma^{(r)},\bar{\mathbf{q}}^{(r)}}\right)^{T} \tag{28}$$

$$<\delta\dot{\boldsymbol{\omega}}^{t(\delta\sigma)} \otimes \delta\dot{\boldsymbol{\omega}}^{t(\delta r)}>^{(r)} = \frac{\partial\dot{\boldsymbol{\omega}}}{\partial\boldsymbol{\sigma}}\Big|^{t}_{\sigma^{(r)},\bar{\mathbf{q}}^{(r)}} <\delta\boldsymbol{\sigma}^{t} \otimes \delta\mathbf{r}^{t}>^{(r)} \left(\frac{\partial\dot{\boldsymbol{\omega}}}{\partial\delta\mathbf{r}}\Big|^{t}_{\sigma^{(r)},\bar{\mathbf{q}}^{(r)}}\right)^{T}, \tag{29}$$

where the cross-covariance $<\delta\boldsymbol{\sigma}^{t} \otimes \delta\mathbf{r}^{t}>^{(r)}$ is given by:

$$<\delta\boldsymbol{\sigma}^{t} \otimes \delta\mathbf{r}^{t}>^{(r)} = <\delta\boldsymbol{\sigma}^{t(\bar{q})} \otimes \delta\mathbf{r}^{t}>^{(r)} + \frac{\partial\boldsymbol{\sigma}}{\partial\delta\mathbf{r}}\Big|^{t}_{\sigma^{(r)},\bar{\mathbf{q}}^{(r)}} <\delta\mathbf{r}^{t} \otimes \delta\mathbf{r}^{t}>^{(r)}. \tag{30}$$

2.4. Misorientation fluctuations

Next, an algorithm for integration of lattice spin fluctuations and updating of second moments of misorientation vectors from time t to time $t + \Delta t$ is described (Zecevic et al., 2017). The updated orientation at material point $\mathbf{x}$ and time, $t + \Delta t$, is given by:

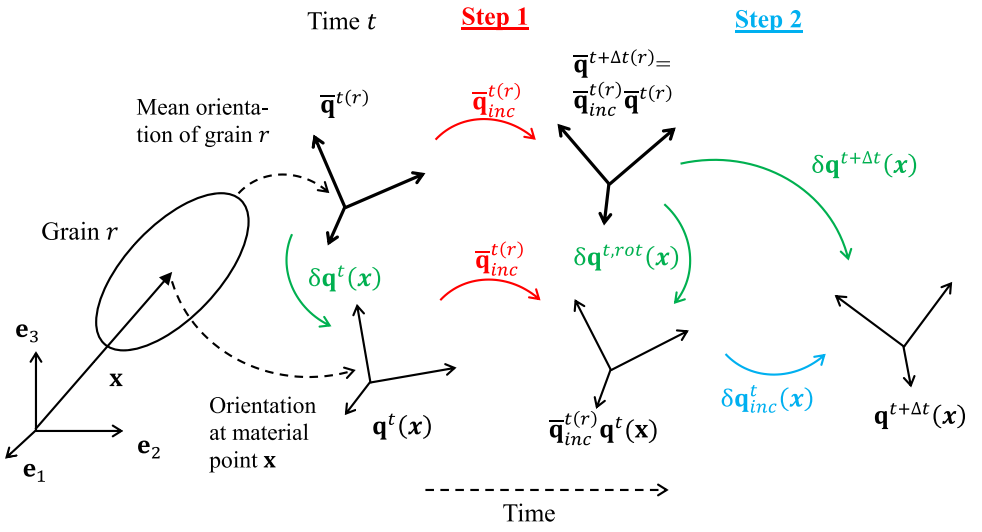

Fig. 1. Evolution of: (1) the mean grain orientation, (2) the orientation at a material point **x** and (3) the misorientation at the material point **x** during orientation update from time t to time $t + \Delta t$. The increment in rotation is decomposed into two rotations: the mean increment in rotation, $\bar{\mathbf{q}}^{t(r)}_{inc}$, and the increment in misorientation, $\delta\mathbf{q}^{t}_{inc}(\mathbf{x})$, which are applied sequentially in two steps.

$$\mathbf{q}^{t+\Delta t}(\mathbf{x}) = \mathbf{q}^{t}_{inc}(\mathbf{x})\mathbf{q}^{t}(\mathbf{x}), \tag{31}$$

where $\mathbf{q}^{t}_{inc}(\mathbf{x})$ represents the increment in rotation at material point **x** and time t and $\mathbf{q}^{t}(\mathbf{x})$ and $\mathbf{q}^{t+\Delta t}(\mathbf{x})$ are the active rotations rotating the sample frame to local crystal frame at t and $t + \Delta t$. The orientations $\mathbf{q}^{t}(\mathbf{x})$ and $\mathbf{q}^{t+\Delta t}(\mathbf{x})$ can be written as composition of the corresponding mean grain orientations, $\bar{\mathbf{q}}^{t(r)}$ and $\bar{\mathbf{q}}^{t+\Delta t(r)}$, and the local misorientations at those material points with respect to the corresponding mean orientation of the corresponding grain, $\delta\mathbf{q}^{t+\Delta t}(\mathbf{x})$ and $\delta\mathbf{q}^{t}(\mathbf{x})$:

$$\mathbf{q}^{t}(\mathbf{x}) = \delta\mathbf{q}^{t}(\mathbf{x})\bar{\mathbf{q}}^{t(r)}, \tag{32A}$$

$$\mathbf{q}^{t+\Delta t}(\mathbf{x}) = \delta\mathbf{q}^{t+\Delta t}(\mathbf{x})\bar{\mathbf{q}}^{t+\Delta t(r)}. \tag{32B}$$

In addition, the increment in rotation can also be decomposed into the mean increment in rotation, $\bar{\mathbf{q}}^{t(r)}_{inc}$, and the increment in misorientation defined with respect to that mean increment in rotation, $\delta\mathbf{q}^{t}_{inc}(\mathbf{x})$:

$$\mathbf{q}^{t}_{inc}(\mathbf{x}) = \delta\mathbf{q}^{t}_{inc}(\mathbf{x})\bar{\mathbf{q}}^{t(r)}_{inc}. \tag{33}$$

By substituting Eq. (33) into Eq. (31) we obtain: $\mathbf{q}^{t+\Delta t}(\mathbf{x}) = \delta\mathbf{q}^{t}_{inc}(\mathbf{x})\bar{\mathbf{q}}^{t(r)}_{inc}\mathbf{q}^{t}(\mathbf{x})$. Consequently, the orientation update can be decomposed into two separate steps illustrated on Fig. 1 (Zecevic et al., 2017): 1) Update for the mean increment in rotation, $\bar{\mathbf{q}}^{t(r)}_{inc}$, which is constant within the grain, 2) Update for the increment in misorientation, $\delta\mathbf{q}^{t}_{inc}(\mathbf{x})$. Fig. 1 shows the evolution of mean grain orientation, $\bar{\mathbf{q}}^{t(r)}$, and misorientation at time t, $\delta\mathbf{q}^{t}(\mathbf{x})$, during the two step update of the orientation. In the first step, the mean increment in rotation is applied to the orientation of every material point within the grain. Consequently, the mean orientation of the grain becomes: $\bar{\mathbf{q}}^{t(r)}_{inc}\bar{\mathbf{q}}^{t(r)}$. Since the same increment in rotation, $\bar{\mathbf{q}}^{t(r)}_{inc}$, is applied to the orientation of every material point of the grain, $\mathbf{q}^{t}(\mathbf{x})$, and to the mean orientation of the grain, the misorientations between the orientations at material points and the mean orientation physically rotate in the sample frame for $\bar{\mathbf{q}}^{t(r)}_{inc}$: $\delta\mathbf{q}^{t,rot}(\mathbf{x}) = \bar{\mathbf{q}}^{t(r)}_{inc}\delta\mathbf{q}^{t}(\mathbf{x})\bar{\mathbf{q}}^{t(r)-1}_{inc}$.

In the second step, the increments in misorientation, $\delta\mathbf{q}^{t}_{inc}(\mathbf{x})$, are applied to the orientation of every material point. It is assumed that the increments in the misorientation do not affect the mean orientation of the grain since their mean value corresponds to the identity rotation quaternion. Therefore, the mean orientation after the second step remains the same: $\bar{\mathbf{q}}^{t+\Delta t(r)} \approx \bar{\mathbf{q}}^{t(r)}_{inc}\bar{\mathbf{q}}^{t(r)}$. Since the mean orientation remains the same, and since the orientation at each material point is updated for the $\delta\mathbf{q}^{t}_{inc}(\mathbf{x})$, the misorientation between the mean orientation and orientation at material point becomes $\delta\mathbf{q}^{t+\Delta t}(\mathbf{x}) = \delta\mathbf{q}^{t}_{inc}(\mathbf{x})\delta\mathbf{q}^{t,rot}(\mathbf{x})$ (Zecevic et al., 2017). Note that in the first step, the mean increment in the misorientation is applied resulting in the evolution of the mean grain orientation while the misorientations only physically rotate in the sample frame. In contrast, in the second step the increments in misorientation are applied and the mean orientation of the grain remains unaltered while the misorientations evolve to their final values.

By performing a first order Taylor expansion of the expression for the misorientation update, $\delta\mathbf{q}^{t+\Delta t}(\mathbf{x}) = \delta\mathbf{q}^{t}_{inc}(\mathbf{x})\delta\mathbf{q}^{t,rot}(\mathbf{x})$, around the mean grain values with respect to $\delta\mathbf{q}^{t}_{inc}(\mathbf{x})$ and $\delta\mathbf{q}^{t,rot}(\mathbf{x})$, the linearized expression for orientation update is obtained (Zecevic et al., 2017):

$$\delta\mathbf{q}^{t+\Delta t}(\mathbf{x}) \approx \delta\mathbf{q}^{t}_{inc}(\mathbf{x}) + \delta\mathbf{q}^{t,rot}(\mathbf{x}) - \mathbf{I}^{q}, \tag{34}$$

where $\mathbf{I}^{q}$ is the identity rotation quaternion. Eq. (34) can be rewritten in terms of the vector parts of the misorientation quaternions:

$$\delta\mathbf{r}^{t+\Delta t}(\mathbf{x}) = \delta\mathbf{r}^{t,rot}(\mathbf{x}) + \delta\mathbf{r}^{t}_{inc}(\mathbf{x}). \tag{35}$$

The vector part of the rotated misorientation quaternion at time t can be written as $\delta\mathbf{r}^{t,rot}(\mathbf{x}) = \overline{\mathbf{R}}_{inc}^{t(r)}\delta\mathbf{r}^{t}(\mathbf{x})$, where $\overline{\mathbf{R}}_{inc}^{t(r)}$ is the mean increment in rotation written in the rotation matrix representation. The vector part of the incremental rotation quaternion is approximated as:

$$\delta\mathbf{r}_{inc}^{t}(\mathbf{x}) \approx \frac{\delta\dot{\omega}^{t}(\mathbf{x})}{|\delta\dot{\omega}^{t}(\mathbf{x})|}\sin\left(\frac{|\delta\dot{\omega}^{t}(\mathbf{x})|\Delta t}{2}\right). \tag{36}$$

By assuming a small angle approximation, $\sin\theta \approx \theta$, the above equation can be simplified to:

$$\delta\mathbf{r}_{inc}^{t}(\mathbf{x}) \approx \delta\dot{\omega}^{t}(\mathbf{x})\frac{\Delta t}{2}. \tag{37}$$

The second moment of the vector part of the misorientation quaternion at time $t + \Delta t$ is given by:

$$<\delta\mathbf{r}^{t+\Delta t} \otimes \delta\mathbf{r}^{t+\Delta t}>^{(r)} = <\delta\mathbf{r}_{inc}^{t} \otimes \delta\mathbf{r}_{inc}^{t}>^{(r)} + <\delta\mathbf{r}^{t,rot} \otimes \delta\mathbf{r}_{inc}^{t}>^{(r)} + <\mathbf{r}_{inc}^{t} \otimes \delta\mathbf{r}^{t,rot}>^{(r)} + <\delta\mathbf{r}^{t,rot} \otimes \delta\mathbf{r}^{t,rot}>^{(r)}, \tag{38}$$

where the individual terms on the right hand side are:

$$<\delta\mathbf{r}_{inc}^{t} \otimes \delta\mathbf{r}_{inc}^{t}>^{(r)} = \frac{\Delta t^2}{4} <\delta\dot{\omega}^{t} \otimes \delta\dot{\omega}^{t}>^{(r)} \tag{39}$$

$$<\delta\mathbf{r}^{t,rot} \otimes \delta\mathbf{r}^{t,rot}>^{(r)} = \overline{\mathbf{R}}_{inc}^{t(r)} <\delta\mathbf{r}^{t} \otimes \delta\mathbf{r}^{t}>^{(r)} \overline{\mathbf{R}}_{inc}^{t(r)^T} \tag{40}$$

$$<\delta\mathbf{r}^{t,rot} \otimes \delta\mathbf{r}_{inc}^{t}>^{(r)} = \overline{\mathbf{R}}_{inc}^{t(r)} <\delta\mathbf{r}^{t} \otimes \delta\sigma^{t}>^{(r)} \left(\frac{\partial\dot{\omega}}{\partial\sigma}\Big|_{\sigma^{(r)},\bar{\mathbf{q}}^{(r)}}^{t}\right)^{T}\frac{\Delta t}{2} + \overline{\mathbf{R}}_{inc}^{t,(r)} <\delta\mathbf{r}^{t} \otimes \delta\mathbf{r}^{t}>^{(r)} \left(\frac{\partial\dot{\omega}}{\partial\delta\mathbf{r}}\Big|_{\sigma^{(r)},\bar{\mathbf{q}}^{(r)}}^{t}\right)^{T}\frac{\Delta t}{2}. \tag{41}$$

2.5. Approximation of the cross-covariance $<\delta\sigma^{t(\bar{q})} \otimes \delta\mathbf{r}^{t}>^{(r)}$

Term $<\delta\sigma^{t(\bar{q})} \otimes \delta\mathbf{r}^{t}>^{(r)}$ represents the cross-covariance between two fundamental sources of fluctuations: stress fluctuations caused by the spatial variation of the mean crystal properties from grain to grain, $\delta\sigma^{t(\bar{q})}$, and the intragranular misorientation fluctuations, $\delta\mathbf{r}^{t}$. Consequently, the cross-covariance terms appearing in the expressions for second moments of stress, lattice spin and misorientation vectors can be written in terms of $<\delta\sigma^{t(\bar{q})} \otimes \delta\mathbf{r}^{t}>^{(r)}$ (Eqs. (23), (29), (30) and (41)). Hence, the cross-covariance $<\delta\sigma^{t(\bar{q})} \otimes \delta\mathbf{r}^{t}>^{(r)}$ is the only unknown term in the algorithm outlined above. Let us assume the cross-covariance $<\delta\sigma^{t-\Delta t(\bar{q})} \otimes \delta\mathbf{r}^{t-\Delta t}>^{(r)}$ at time $t - \Delta t$ is known. We propose an algorithm for calculation of the cross-covariance $<\delta\sigma^{t(\bar{q})} \otimes \delta\mathbf{r}^{t}>^{(r)}$ at time t based on an incremental update of the cross-covariance at time $t - \Delta t$.

First, let us assume a linear relation between stress fluctuations at times $t - \Delta t$ and t:

$$\delta\sigma^{t(\bar{q})}(\mathbf{x}) = \mathbf{Z}^{(r)}\delta\sigma^{t-\Delta t(\bar{q})}(\mathbf{x}), \tag{42}$$

where matrix $\mathbf{Z}^{(r)}$ defines the relation between stress fluctuations from two subsequent time increments in grain r. Calculation of matrix $\mathbf{Z}^{(r)}$ is given in Appendix B. By using Eqs. (24), (35) and (36), the misorientation at time t can be written as a linear function of $\delta\sigma^{t-\Delta t(\bar{q})}$ and $\delta\mathbf{r}^{t-\Delta t}$:

$$\delta\mathbf{r}^{t}(\mathbf{x}) = \mathbf{Y}^{(\delta r)(r)}\delta\mathbf{r}^{t-\Delta t}(\mathbf{x}) + \mathbf{Y}^{(\delta\sigma)(r)}\delta\sigma^{t-\Delta t(\bar{q})}(\mathbf{x}), \tag{43}$$

where matrices $\mathbf{Y}^{(\delta r)(r)}$ and $\mathbf{Y}^{(\delta\sigma)(r)}$ are given by:

$$\mathbf{Y}^{(\delta r)(r)} = \frac{\Delta t}{2}\frac{\partial\dot{\omega}}{\partial\sigma}\Big|_{\sigma^{(r)},\bar{\mathbf{q}}^{(r)}}^{t-\Delta t}\frac{\partial\sigma}{\partial\delta\mathbf{r}}\Big|_{\sigma^{(r)},\bar{\mathbf{q}}^{(r)}}^{t-\Delta t} + \frac{\Delta t}{2}\frac{\partial\dot{\omega}}{\partial\delta\mathbf{r}}\Big|_{\sigma^{(r)},\bar{\mathbf{q}}^{(r)}}^{t-\Delta t} + \mathbf{R}_{inc}^{t-\Delta t(r)}, \tag{44}$$

$$\mathbf{Y}^{(\delta\sigma)(r)} = \frac{\Delta t}{2}\frac{\partial\dot{\omega}}{\partial\sigma}\Big|_{\sigma^{(r)},\bar{\mathbf{q}}^{(r)}}^{t-\Delta t}. \tag{45}$$

Eq. (43) illustrates the previous observation that an intragranular fluctuation of any variable stems from the two fundamental sources: intragranular fluctuations of stress due to variation of mean grain properties within the polycrystal, $\delta\sigma^{t-\Delta t(\bar{q})}(\mathbf{x})$, and intragranular fluctuations of misorientation, $\delta\mathbf{r}^{t-\Delta t}(\mathbf{x})$. Substituting Eqs. (42) and (43) into cross-covariance $<\delta\sigma^{t(\bar{q})} \otimes \delta\mathbf{r}^{t}>^{(r)}$ yields:

$$<\delta\sigma^{t(\bar{q})} \otimes \delta\mathbf{r}^{t}>^{(r)} = \mathbf{Z}^{(r)} <\delta\sigma^{t-\Delta t(\bar{q})} \otimes \delta\mathbf{r}^{t-\Delta t}>^{(r)} (\mathbf{Y}^{(\delta r)(r)})^{T} + \mathbf{Z}^{(r)} <\delta\sigma^{t-\Delta t(\bar{q})} \otimes \delta\sigma^{t-\Delta t(\bar{q})}>^{(r)} (\mathbf{Y}^{(\delta\sigma)(r)})^{T}. \tag{46}$$

Eq. (46) defines the cross-covariance $<\delta\sigma^{t(\bar{q})} \otimes \delta\mathbf{r}^{t}>^{(r)}$ as a function of cross-covariance from time $t - \Delta t$.

2.6. Grain fragmentation model

Let us consider one grain with a given mean orientation, $\bar{\mathbf{q}}^{(r)}$, and associated second moment of misorientation vectors, $<\delta\mathbf{r} \otimes \delta\mathbf{r}>^{(r)}$. During deformation, the misorientation spread will generally increase and, at a certain strain, it may become so large that it cannot be represented accurately with only one mean value and one second moment. In addition, the spread may become so large that it is no longer reasonable to assume that the behavior of the grain is defined solely by the mean orientation of the grain.

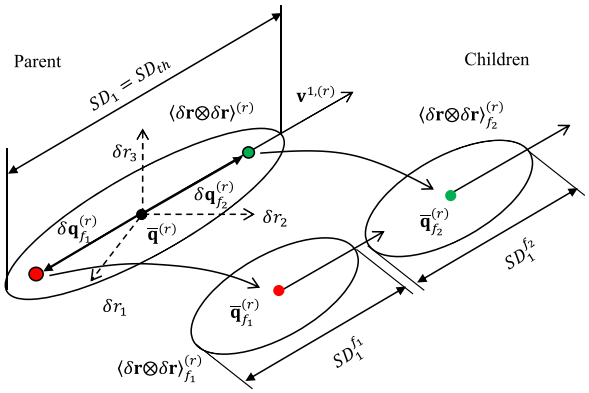

Fig. 2. Fragmentation of the parent grain into two child grains when the standard deviation, SD_1, along the direction of largest variation, $\mathbf{v}^1$, reaches the threshold value, SD_{th}. The orientations of the child grains, $\bar{\mathbf{q}}_{f_1}^{(r)}$ and $\bar{\mathbf{q}}_{f_2}^{(r)}$, are defined based on the parents mean orientation, $\bar{\mathbf{q}}^{(r)}$, and misorientation distribution, $<\delta\mathbf{r} \otimes \delta\mathbf{r}>^{(r)}$ (Appendix C). Mean orientations of the children grains are misoriented with respect to the mean orientation of the parent around the axis aligned with the vector $\mathbf{v}^1$. The misorientation distributions are represented by iso-density ellipsoids.

Furthermore, the Taylor expansion with respect to the misorientation vectors around the mean grain orientation, holds only for reasonably small misorientation vectors. Therefore, a grain fragmentation model becomes necessary when considering deformation to higher strains.

In order to quantify the magnitude of the misorientation spread, we calculate the principal values, λ^i, and directions, $\mathbf{v}^i$, of the misorientation distribution, $<\delta\mathbf{r} \otimes \delta\mathbf{r}>^{(r)}$, and sort them in descending order (Pantleon, 2005). The matrix $<\delta\mathbf{r} \otimes \delta\mathbf{r}>^{(r)}$ is a covariance matrix and thus has to be positive-semidefinite by definition, implying that the eigenvalues are non-negative: $\lambda^i \geq 0$. The maximum principal value, λ^1, represents the variance along the corresponding principal direction of largest variation, $\mathbf{v}^1$. The standard deviations along principal directions are defined as $SD_i = \sqrt{\lambda^i}$. For the purposes of the fragmentation model, the misorientation distribution is assumed to be multivariate normal.

Misorientation vectors along the direction $\mathbf{v}^1$ are the largest in the misorientation distribution and thus the Taylor expansion of stress and spin (Eqs. (20) and (24)) might not be sufficiently accurate for these misorientation vectors. In addition, the additive accumulation of misorientation vectors (Eq. (35)) holds only for relatively small misorientations. Therefore, when the largest standard deviation, SD_1, reaches a critical value, SD_{th}, further evolution of the intragranular distributions becomes inaccurate. One solution to this problem is division of the grain into two child grains once SD_1 reaches critical value (Fig. 2). The mean orientations of the children grains, $\bar{\mathbf{q}}_{f_1}^{(r)}$ and $\bar{\mathbf{q}}_{f_2}^{(r)}$, are calculated by misorienting the mean orientation of the parent grain, $\bar{\mathbf{q}}^{(r)}$, around the direction of largest variation, $\mathbf{v}^1$, for an angle calculated based on the SD_1 (see Appendix C). The misorientation distributions of children grains are calculated by dividing the parent's misorientation distribution along the direction of largest variation, $\mathbf{v}^1$ (see Appendix C). From all the possible divisions of the parent's misorientation distribution, division along the direction of largest variation gives the fragmented distributions with the smallest maximal standard deviations, $SD_1^{f_1}$ and $SD_1^{f_2}$. Consequently, the Taylor expansion around the mean orientation and the additive accumulation of misorientation vectors hold again for the children grains. The misorientation distributions of the parent grain and children grains are illustrated by iso-density ellipsoids in Fig. 2. Points on the surface of the iso-density ellipsoid have the same probability density. For illustration purposes, the semi axes of iso-density ellipsoids are chosen to correspond to the standard deviations, SD_i. Since the slip resistance is assumed constant within the grain, the children grains inherit the parent's slip resistance. The mean stress and strain rate within the children are also assumed same as parent's and they only serve as initial guesses for the next time increment when they will be calculated by means of the self-consistent procedure.

The threshold value for SD_1 is suitably chosen so that the angle between the mean orientations of the children grains is 15° at the moment of fragmentation. On one hand, higher threshold value for SD_1 might result in reduced accuracy, while on the other hand lower threshold value for SD_1 would give more accurate result but would also cause more excessive fragmentation and very large number of fragments at higher strains. The chosen value is a compromise that yields accurate results and manageable number of grains even at higher strains.

3. Results and discussion

The GF-VPSC model for prediction of intragranular misorientation spreads is applied to tension of an fcc polycrystal at room temperature, and PSC of an fcc polycrystal at elevated temperature. The predictions are compared to VPFFT full-field (Lebensohn, 2001; Lebensohn et al., 2008) simulation results for the case of tension, and to both VPFFT and experimental results (Quey et al., 2010 for rolled Al) in the case of PSC. In addition, coupling of deformation and recrystallization modeling is discussed at the end of this section.

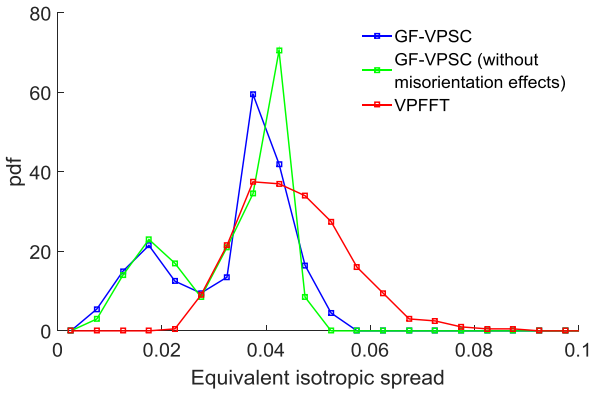

Fig. 3. Probability density functions (pdf) of equivalent isotropic spreads calculated using GF-VPSC, GF-VPSC without misorientation effects, and VPFFT, for an fcc polycrystal deformed in tension to 40% strain.

3.1. Uniaxial tension of an fcc polycrystal

Uniaxial tension of a polycrystal consisting of 400 spherical, randomly oriented grains is simulated to 40% strain using the GF-VPSC model and compared with full-field VPFFT predictions. The initial microstructure for full-field VPFFT simulation was created by assigning the 400 random orientations used in GF-VPSC simulations to 400 approximately equiaxed and equal-volume grains within a periodic Voronoi unit cell. The grains are assumed to deform by $\{111\}<1\bar{1}0>$ slip with a power-law exponent in Eq. (2) of $n = 10$, and no strain hardening. In addition, the same deformation is simulated with the VPSC model used in (Zecevic et al., 2017). The grain fragmentation scheme described in section 2.6 was implemented in this earlier model as well, in order to facilitate the comparison. The VPSC model reported in (Zecevic et al., 2017) calculates intragranular misorientation distributions based on the second moments of lattice rotation rates (Lebensohn et al., 2016) in a similar manner to the GF-VPSC model, but does not include the effects of the misorientation distributions on the stress and lattice spin fluctuations. Consequently, the difference between the results of the two VPSC predictions shows the importance of considering the effects of the misorientation on the fluctuations of stress and lattice spin.

The magnitude of the orientation spread for each grain within the polycrystal can be quantified with one scalar parameter: equivalent isotropic spread. Consequently, a discrete set of grain equivalent isotropic spreads can be created for a polycrystal and a probability density (pdf) function of the equivalent isotropic spreads can be defined. Fig. 3 shows the pdfs of the equivalent isotropic spreads calculated over the polycrystal for GF-VPSC, GF-VPSC without misorientation effects on fluctuations, and VPFFT. The equivalent isotropic spread, SD, is calculated as the geometric mean of the standard deviations, SD_i, along the principal directions of the intragranular misorientation spread: $SD = \sqrt[3]{SD_1 \times SD_2 \times SD_3}$ (Krog-Pedersen et al., 2009). The standard deviations, SD_i, can be used for construction of iso-density ellipsoids around the mean grain value of misorientation vectors, $<\delta\mathbf{r}>^{(r)} = \mathbf{0}$. Misorientation vectors pointing to the surface of the iso-density ellipsoid are exactly one standard deviation away from the grain's mean of the misorientation vectors, and their probability density is the same. Equivalent isotropic spread represents a radius of a sphere which has the same volume as the defined iso-density ellipsoid and thus represents standard deviation of the isotropic spread defined based on the anisotropic misorientation distribution. A majority of grains in the VPFFT model develop equivalent isotropic spreads around 0.045 with relatively high dispersion. On the other hand, both GF-VPSC models predict strong concentration of equivalent isotropic spreads around 0.04 and weaker concentration around 0.02. The presence of an additional peak in the GF-VPSC pdf predictions is caused by the disc shaped misorientation distributions in the grains with tensile axis close to [001]. Very small magnitude of standard deviation along the direction of smallest variation, SD_3, results in an unreasonably small magnitude of the equivalent isotropic spreads within those grains (Zecevic et al., 2017). Main cause for development of such misorientation distributions is the insensitivity of spin component along the tension direction to the fluctuations in stress, as will be detailed below. Considering the discrepancy between the GF-VPSC and VPFFT, we conclude that the Taylor expansion of spin with respect to stress becomes inaccurate for orientations with the tensile direction (TD) close to [001].

The direction of the misorientation distribution of each grain in the polycrystal can be quantified with one vector pointing in the direction of the largest variation, i.e. the dominant rotation axis. Fig. 4 compares the equal-area projections of dominant rotation axes between GF-VPSC, GF-VPSC without misorientation effects on fluctuations, and VPFFT, for all of the grains in the polycrystal. The largest variation of intragranular misorientation spread is about the dominant rotation axis, aligned with the direction of the eigenvector, $\mathbf{v}^1$, corresponding to largest eigenvalue, λ^1, of the second moment of misorientation, $<\delta\mathbf{r}^t \otimes \delta\mathbf{r}^t>^{(r)}$ (Bachmann et al., 2010; Pantleon, 2005). Physically, the orientations from the grain's orientation spread which are the most misoriented with respect to the mean grain orientation have the axis of misorientation aligned with the dominant rotation axis. For VPFFT, large portion of dominant rotation axes tends to align perpendicular to the TD while the remaining portion is randomly spread out around TD. Similarly, GF-VPSC predicts strong alignment of the dominant rotation axes perpendicular to TD. In addition, GF-VPSC predicts a certain portion of dominant rotation axes relatively close to TD but in a ring about 30° away from the TD. On the other hand, the GF-VPSC model without effects of misorientation on fluctuations predicts all the axes to be perpendicular to the TD. In addition, the

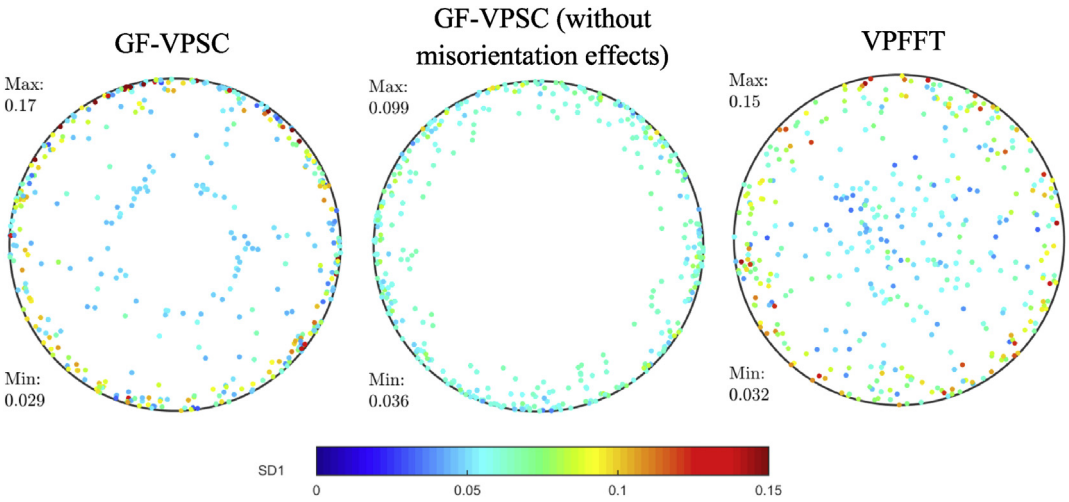

Fig. 4. Comparison of dominant rotation axes calculated using GF-VPSC, GF-VPSC without misorientation effects, and VPFFT, after tension to 40% strain, color-coded according to magnitude of standard deviation along dominant rotation axis. (For interpretation of the references to color in this figure legend, the reader is referred to the Web version of this article.)

magnitudes of SD along the dominant rotation axes in the GF-VPSC simulations without effects of misorientation are generally smaller than the magnitudes observed in the GF-VPSC and VPFFT simulations. In both GF-VPSC and VPFFT simulations, grains with the dominant rotation axis perpendicular to TD tend to develop higher SD in comparison to the grains with the dominant rotation axis parallel to TD.

Fig. 5 shows the orientation dependence of the angle between the dominant rotation axis and TD for GF-VPSC, GF-VPSC without misorientation effects on fluctuations, and VPFFT. For VPFFT, the axes displaying the smallest angles are for orientations close to the stable orientations, [001] and [111]. On the other hand, GF-VPSC predicts the smallest angle only in the region close to [111] but not directly at [111]. The GF-VPSC without misorientation effects on fluctuations predicts an angle close to 90° for all of the grains, as expected based on Fig. 4. Therefore, the rotation of dominant rotation axes toward TD in GF-VPSC is likely caused by the introduced effects of misorientation on the stress and lattice spin fluctuations. The observed behavior for VPFFT and GF-VPSC is analyzed in detail next.

During the initial stages of tensile loading, grains develop misorientation spreads perpendicular to TD both in GF-VPSC and VPFFT (Zecevic et al., 2017). Lattice spin fluctuations can be decomposed into fluctuations caused by: i) intragranular stress fluctuations, and ii) intragranular misorientation. The fluctuations of lattice spin at lower strains are predominantly driven by the stress fluctuations, since intragranular misorientations are fairly small. The component of lattice spin along TD is less sensitive to stress fluctuations than the other two components lying in the plane perpendicular to the TD, which causes intragranular misorientation spreads to develop perpendicular to TD (Zecevic et al., 2017). This behavior is especially pronounced for orientations with TD within 15° from [001] and 5° from [111] in the GF-VPSC results, for which variations of intragranular misorientation spreads along TD are very small.

At higher strains, the influence of the intragranular misorientation on lattice spin fluctuations becomes dominant due to large

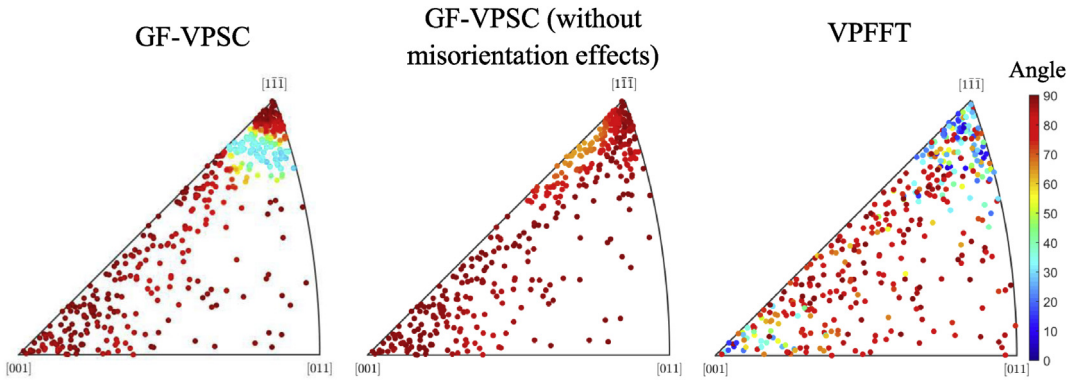

Fig. 5. Inverse pole figures after tension to 40% strain for GF-VPSC, GF-VPSC without misorientation effects, and VPFFT. The poles represent the orientation of TD in the crystal frame of each grain, and their colors represent the angles between the dominant rotation axis and the tensile direction. (For interpretation of the references to color in this figure legend, the reader is referred to the Web version of this article.)

misorientation spreads. When a grain with a certain orientation spread reaches either the [001] || TD or [111] || TD stable fibers, the lattice spin fluctuations of the orientations within the spread that are away from the fiber cause reorientation toward the fiber, since the region around the fiber is convergent. On the other hand, lattice spin fluctuations of orientations of the spread that are on the fiber cause very small total reorientations since these intragranular orientations have reached a stable position. Therefore, orientation spreads of these grains tend to assume the shape of the fiber. Similar behavior was observed during PSC of fcc polycrystals (Quey et al., 2015). Consequently, as the grains approach [001] and [111] regions, they start developing misorientation spread with dominant rotation axis parallel to TD because their orientation spread tends to align with the stable fiber. This behavior is observed in VPFFT and is more pronounced around [111] than in the [001] region because orientations tend to converge to [111] faster than to [001] (Lebensohn et al., 2016).

In GF-VPSC, orientations that are initially close to the stable regions [111] and [001] develop very small spreads along TD, as was noted before. The lattice spin fluctuations caused by the intragranular misorientation tend to shrink the spread in the plane perpendicular to TD and thus bring all the orientations of the spread to the fiber. However, regardless of this effect, the dominant rotation axis will remain perpendicular to TD because variations of the intragranular misorientation spread along TD are very small. Only orientations with [111] about 10° away from TD develop sufficiently large components of misorientation spread along TD. Consequently, only these orientations show the dominant rotation axis close to TD as they reorient toward the [111] due to the effect of the plastic spin fluctuations caused by the intragranular misorientation (Fig. 5).

3.2. PSC of fcc polycrystal at elevated temperature

Quey et al. (2010) performed PSC of recrystallized Al-0.1 wt%Mn at 400 °C to a final rolling strain of 1.2. The same region of the sample was scanned using EBSD at strain levels of 0.0, 0.42, 0.77 and 1.2. The grains present in the EBSD scan of the initial microstructure were identified in the subsequent scans taken at each strain level. Therefore, the intragranular orientation spread of this subset of grains is available at each strain level. In addition, crystal plasticity finite element (CPFE) modeling of the experiment and analysis of misorientation spreads was performed in (Quey et al., 2012, 2015).

We simulated Quey et al.'s PSC experiment using the GF-VPSC and VPFFT models, using the orientations of 207 grains present in the initial EBSD scan, along with 193 random orientations as the initial texture. The orientations from the initial texture were sorted according to the volume fraction and assigned to the grains within the periodic Voronoi unit cell that was used as the initial microstructure for the VPFFT simulation. The orientation with the largest volume fraction within the initial texture was assigned to the grain with the largest volume fraction within the Voronoi unit cell, etcetera. This method of orientation assignment ensures the smallest difference between the initial texture of the Voronoi unit cell for VPFFT simulations and the initial texture used in GF-VPSC simulations. There was no intragranular misorientation spread within the initial microstructure. At elevated temperature, the slip resistances of non-octahedral slip systems may drastically decrease resulting in their activation (Bacroix and Jonas, 1988). The slip on non-octahedral planes is interpreted as cross-slip from the plane {111}. Perocheu and Driver measured the stress strain response of Al-1wt%Mn single crystals at 400–500 °C and at different strain rates (Perocheau and Driver, 2002). The orientations of single crystals were chosen to favor different slip systems and slip trace analysis revealed activation of non-octahedral slip systems. The ratios of flow stresses between the $\{111\}\langle 0\bar{1}1\rangle$, $\{011\}\langle 0\bar{1}1\rangle$ and $\{100\}\langle 0\bar{1}1\rangle$ slip modes were determined to be: 1.0-0.9-1.4, respectively. Consequently, in both GF-VPSC and VPFFT models we assume same slip systems with the measured ratio of slip resistances. The rate sensitivity of the flow stress was measured to be between 0.07 and 0.11 (Perocheau and Driver, 2002). In both models we assume rate exponent in the rate-sensitive constitutive equation as $n = 10$ and no strain hardening. The same slip modes and slip resistance ratios and similar rate exponent ($n \approx 8$) were used for the CPFE modeling performed in (Quey et al., 2012; Quey et al., 2015). Comparisons of intragranular misorientation distributions were performed for the subset of grains represented in the EBSD scans with at least 500 points at each strain level, resulting in 119 grains. Since the highly deformed grains are more difficult to index during EBSD scanning at higher strains, the highly deformed grains with relatively small area are less likely to be included in the defined subset of grains which thus might be biased toward less deformed grains. However, since the main purpose of this study is comparison of the model predictions with the experiment for the defined subset of grains, this effect can be neglected.

During deformation, certain grains in the divergent regions of the orientation space subdivide into two distinct portions. Due to different slip activity, one portion of the grain reorients toward one stable region while the other portion of the grain reorients towards a different stable region. These highly misoriented portions of the grain are called deformation bands. Thin regions between the deformation bands are called transition bands, and large orientation difference between the deformation bands is accommodated within them (Dillamore and Katoh, 1974; Hansen and Jensen, 1999). Orientation spread of such grain is bi-modal and consists of orientations clustered around two distinct modes which lie in different stable regions of the orientation space (Quey et al., 2012). Since the grain's misorientation spread simply represents the grain's orientation spread defined with respect to the mean orientation, the misorientation distribution is bi-modal as well (Fig. 6a). The dominant rotation axis of the bi-modal grain describes the misorientation axis between the two modes of the misorientation distribution. The pdf of the misorientation vector components along the dominant rotation axis is again bi-modal and can be used for identification of the bi-modal grains, Fig. 6b (Quey et al., 2012). The misorientations clustered around different modes of the misorientation distribution correspond to different deformation bands (Fig. 6b). On the other hand, the misorientations from the region between the modes of the misorientation distributions correspond to the transition band (Fig. 6b). Therefore, by examining the intragranular misorientation spreads, we can identify grains that developed transition bands and the orientations present in transition bands. The calculated fractions of bi-modal grains at each strain level in the experiment and the simulations are compared in Fig. 7. VPFFT over-predicts the number of bi-modal grains, while GF-VPSC under-predicts it. The CPFE simulations performed in (Quey et al., 2012) predicted a similar fraction of bi-modal grains as VPFFT.

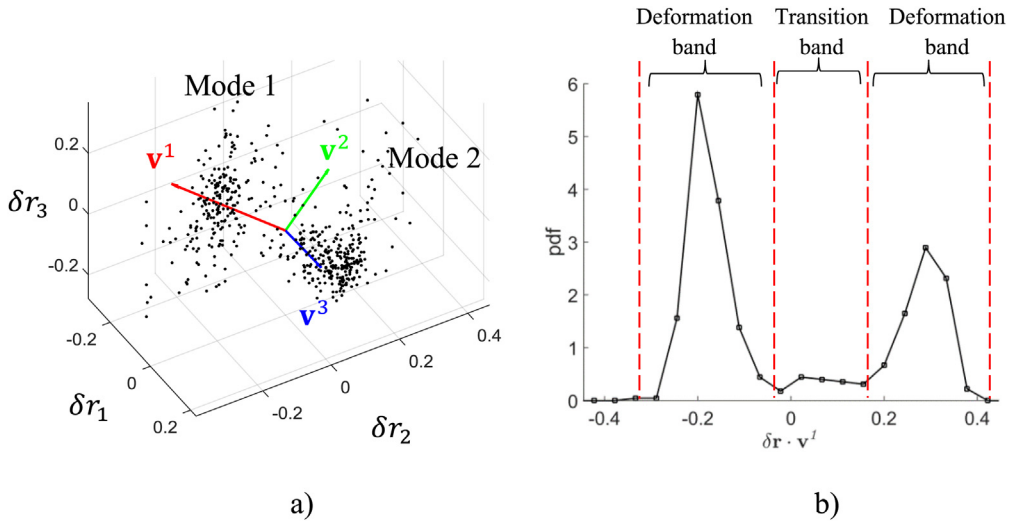

Fig. 6. (a) Scatter plot of misorientation vectors for a bi-modal grain predicted with VPFFT for plane-strain compression, and (b) probability density function of misorientation vector projections along the dominant rotation axis. The principal vectors of misorientation distribution are denoted as $\mathbf{v}^i$.

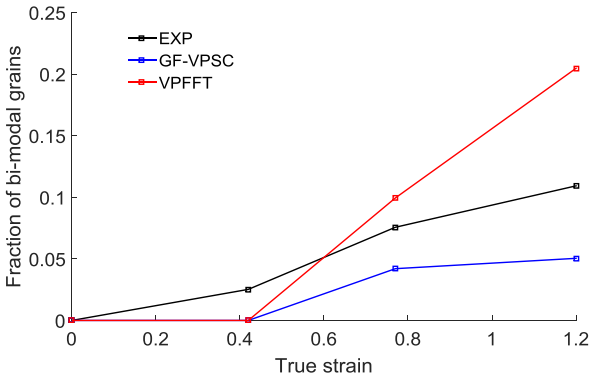

Fig. 7. Comparison between measured (rolled Al) and predicted (GF-VPSC and VPFFT) fractions of bi-modal grains at different strain levels for plane-strain compression.

Grains with bi-modal orientation distributions usually have quite large misorientations between the individual modes, and thus should not be treated as a single grain. As noted above, the dominant rotation axis of the bi-modal grains essentially describes the misorientation axis between the two modes, while the equivalent isotropic spread describes the magnitude of misorientation between the two modes. The misorientation spreads developing around the individual modes have completely different dominant rotation axes and equivalent isotropic spreads. Consequently, the dominant rotation axes and equivalent isotropic spreads of the misorientation distributions are compared only for the grains with unimodal orientation distribution, as was done in (Quey et al., 2015).

Fig. 8 compares the simulated and experimental pdfs of equivalent isotropic spreads calculated over the entire polycrystal at each strain level. The GF-VPSC tends to over-predict the concentration of equivalent isotropic spreads around certain values, in comparison to the experiment. On the other hand, VPFFT displays too much variation of equivalent isotropic spreads, especially at higher strains, which is consistent with the CPFE simulations performed by (Quey et al., 2015). Initially, the magnitudes of equivalent isotropic spreads increase rapidly with strain in both simulations and experiment. Grains that are initially in divergent regions rapidly develop large misorientation spreads, while grains that are in the stable regions develop misorientation spreads at considerably slower rate. Since initially there is a relatively small number of grains in stable convergent regions, the misorientation spreads develop rapidly for a significant fraction of grains. At higher strains, the equivalent isotropic spreads saturate and do not increase significantly with further deformation, an observation which is especially pronounced in the experimental results (Quey et al., 2010). This is because a majority of grains have reached stable convergent orientations, where the misorientation spreads evolve slowly.

Fig. 9 shows the directions of dominant rotation axes after applying the rolling symmetry for simulations and experiment, at each strain level. At lower strains, the dominant rotation axes tend to align with TD in both simulations and experiment, in agreement with (Pantleon et al., 2008). This tendency is weaker in VPFFT predictions, compared to experiment and GF-VPSC results. As the strain increases, the dominant rotation axes start rotating toward RD in the experimental results. A similar trend, though noticeably weaker, is predicted with GF-VPSC. On the other hand, VPFFT predicts a significant fraction of the axes aligned with ND and in the TD-ND

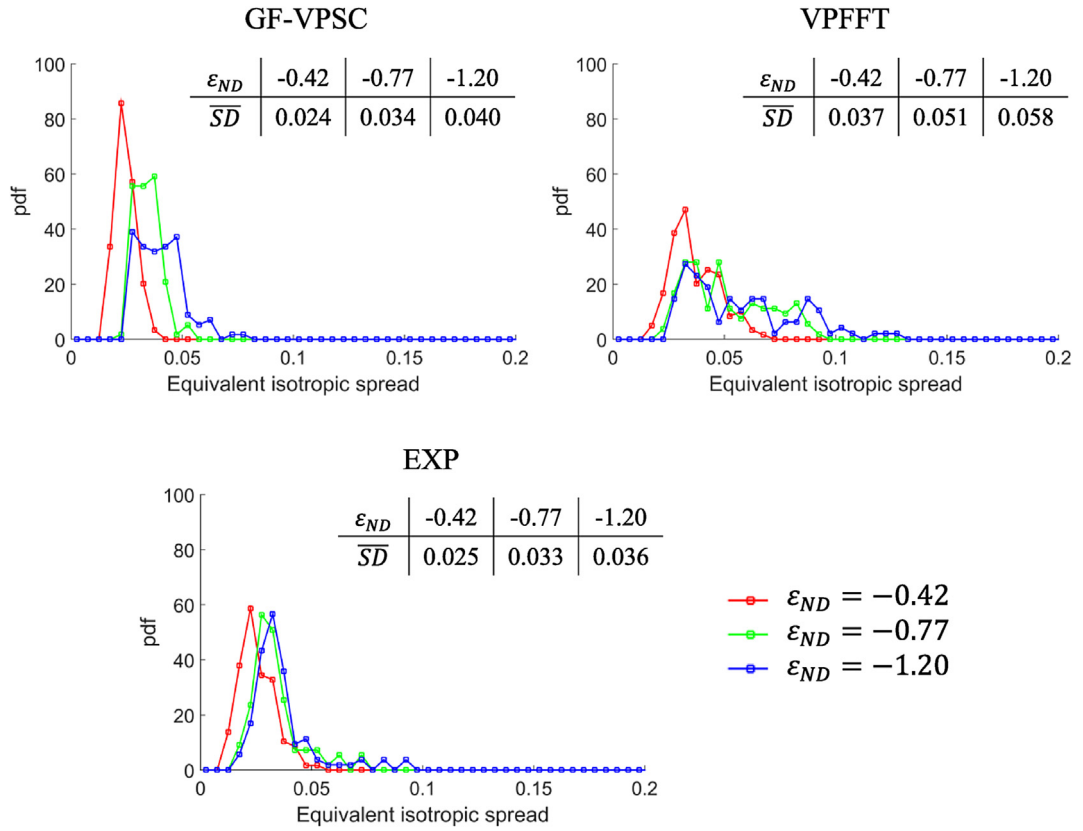

Fig. 8. Experimental (rolled Al) and predicted (GF-VPSC and VPFFT) probability density functions of equivalent isotropic spreads during plane-strain compression at different strain levels. ε_{ND} is the strain in the normal direction while the $\overline{SD} = \frac{1}{n}\sum_r SD^{(r)}$ represents the average value of equivalent isotropic spread over the polycrystal.

plane at higher strains, which is not observed in experiment or GF-VPSC. Similar alignment of the dominant rotation axes with ND was also observed in the CPFE simulations (Quey et al., 2015). This behavior was attributed to the alignment of the misorientation spread with the direction of the fiber to which the mean grain orientation belongs (Quey et al., 2015).

Considering the complexities involved in the physics of grain fragmentation, the GF-VPSC predictions are good. Moreover, the model is much more computationally efficient than the full-field models. The GF-VPSC model without the misorientation effects on the stress and lattice spin fluctuations predicts almost zero bi-modal grains, even at 1.2 strain. In addition, the dominant rotation axes remain strongly aligned with the TD throughout the deformation. These results corroborate our previous assertion, in the sense that field fluctuations caused by the intragranular misorientation become dominant at higher strains.

Both GF-VPSC and VPFFT are three-dimensional (3-D) models, while only two-dimensional (2-D) sections of grains were analyzed in the experiment. Consequently, certain discrepancy between the predictions and measurements is expected (Quey et al., 2015). In addition, the 3-D unit cell used for the VPFFT was generated randomly, solely based on the grain orientations and volume fractions obtained from one 2-D scan of the actual microstructure. Therefore, the generated 3-D unit cell does not correspond to the actual unknown 3-D microstructure of the sample. In the GF-VPSC model, every grain interacts with the effective medium which has the averaged properties of the polycrystal. Consequently, the response of the GF-VPSC model is determined only by the discrete set of grain orientations and volume fractions, while the actual 3-D microstructure corresponding to that set of grains has no influence on the results. In a sense, GF-VPSC gives an averaged response over all possible 3-D microstructures for a defined set of grain orientations and volume fractions (Lebensohn et al., 2004). This statistical representativity can be the explanation for the better agreement of the GF-VPSC model with the experimental results in comparison to the VPFFT. In the absence of the actual 3-D microstructure, averaged response seems to be closer to the experimental measurements than the response of an assumed 3-D microstructure used in VPFFT.

Finally, Fig. 10 compares the textures after deformation in the form of {111} pole figures. The same features are present in both simulations and experiment, but the intensities differ. GF-VPSC predicts a weaker texture than experimentally measured, while VPFFT predicts a peak intensity very close to the experimental value. As a reference, the texture predicted by the VPSC model without the extension for calculation of intragranular misorientation spreads is given in Fig. 10 as well. The predicted peak intensity is considerably higher than the experimentally measured intensity, as was observed in (Lebensohn, 2001), confirming that the incorporation of intragranular misorientation spreads and grain fragmentation improves texture predictions.

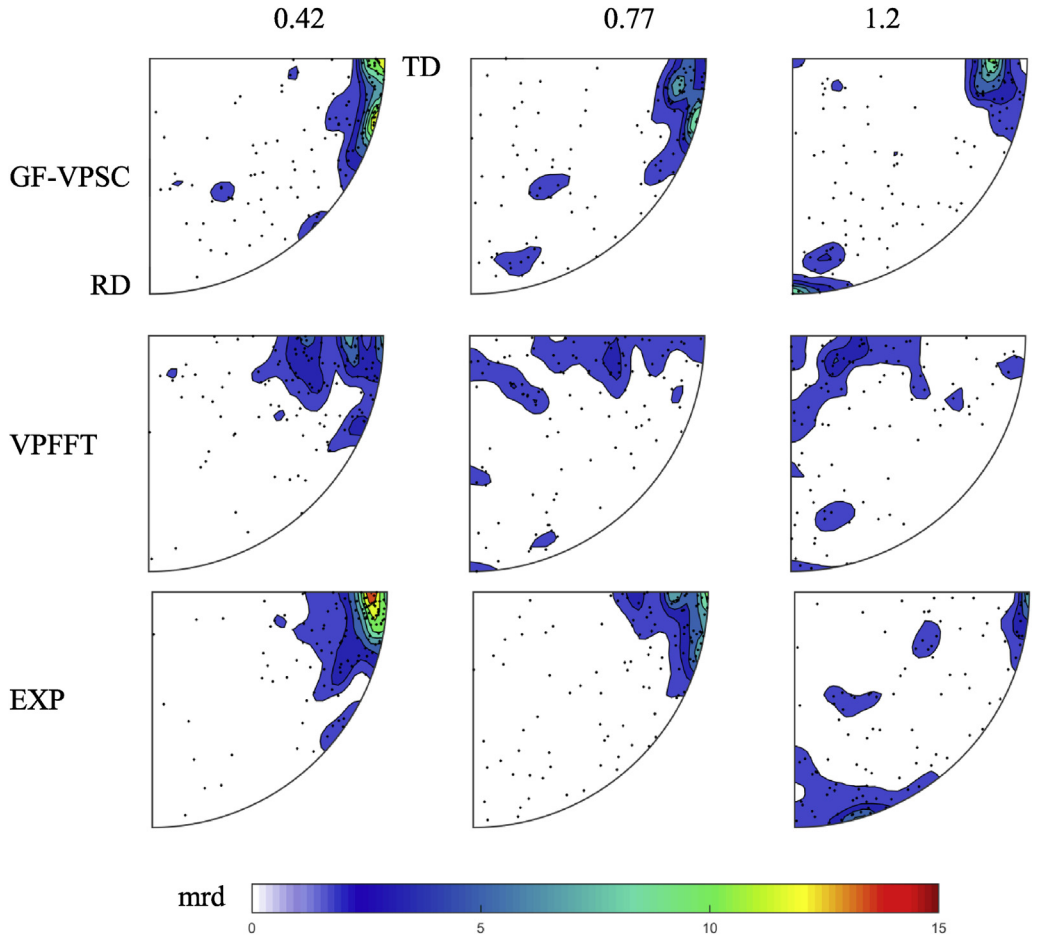

Fig. 9. Dominant rotation axes for experiment (rolled Al) and simulations (GF-VPSC and VPFFT) for plane-strain compression at different strain levels.

3.3. Coupled modeling of deformation and recrystallization

In closing this section, we show that the new GF-VPSC model is not only able to predict grain fragmentation in a micro-mechanically-consistent fashion, and validated by comparison with experiments, but it also enables coupled modeling of microstructure evolution during deformation and recrystallization. As already mentioned, intragranular orientation spreads have been related to the formation of transition bands. These high orientation gradient regions between deformation bands favor recrystallization nuclei, which may have quite different crystallographic orientation compared to the average grain orientation, due to large orientation variations developed in the grains (Ardeljan et al., 2017; Humphreys and Hatherly, 2004; Knezevic et al., 2014, 2016; McCabe et al., 2015). Therefore, even though the GF-VPSC provides only statistical description of intragranular misorientation distributions, in the special case of bi-modal orientation distributions, it can be assumed that the orientations between the modes of the orientation distribution (transition band orientations) spatially neighbor the orientations from the modes of the orientation distribution (deformation band orientations). Consequently, the orientation gradients for these grains become high.

Let us consider the recrystallization of heavily rolled copper, which results in a strong cube texture. It was found that during rolling of copper, certain grains develop transition bands with the cube orientation present within the center of the transition band (Dillamore and Katoh, 1974; Hjelen et al., 1991; Ridha and Hutchinson, 1982). These cube-oriented nuclei grow and consume the deformed microstructure resulting in cube recrystallization texture. In order to simulate this process, GF-VPSC and VPFFT were used to model PSC of copper to a reduction of 78%. The initial microstructure consists of 400 randomly oriented spherical grains deforming by $\{111\}\langle 0\bar{1}1\rangle$ slip with no strain hardening. The grains that have developed bi-modal orientation distributions, and thus formed transition bands, were flagged at the end of deformation, and a *transition-band ODF* was defined by assembling the orientations present within the transition bands of all bi-modal grains. If nucleation at transition bands is accepted as the likely nucleation mechanism, then the transition-band ODF defines possible orientations of recrystallization nuclei. The transition-band ODFs are plotted on Fig. 11 in the form of {111} pole figures as predicted by GF-VPSC and VPFFT. A cube texture is predicted in both cases, in accordance with the previous experimental observations and theoretical considerations and interpretations (Dillamore and Katoh, 1974; Ridha and Hutchinson, 1982).

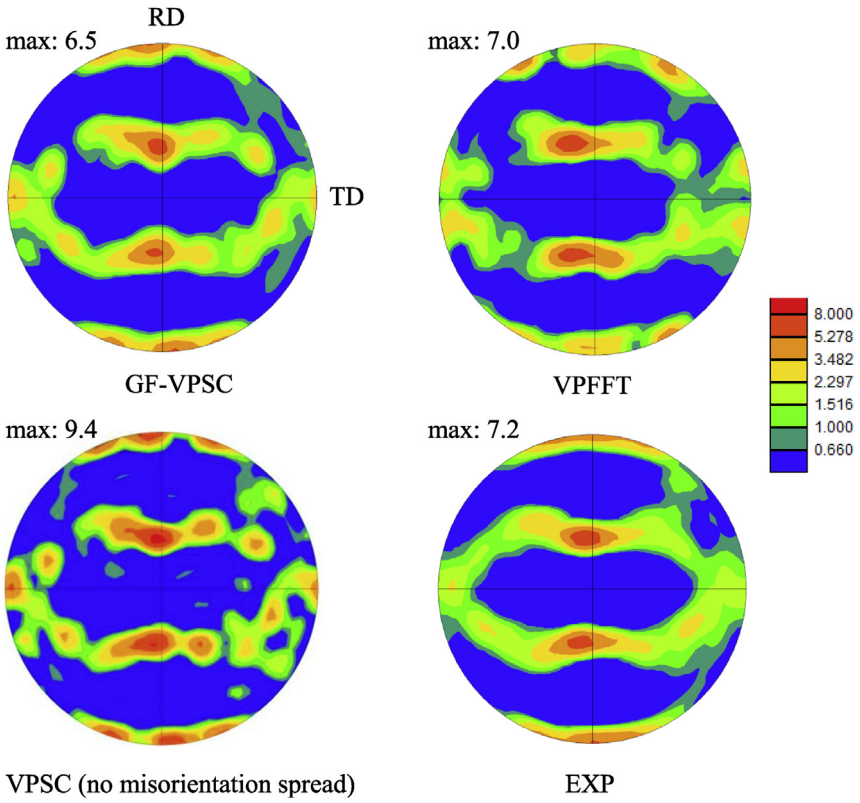

Fig. 10. {111} pole figures measured (rolled Al) and predicted by GF-VPSC, VPFFT, and standard VPSC, for plane-strain compression after 1.2 strain.

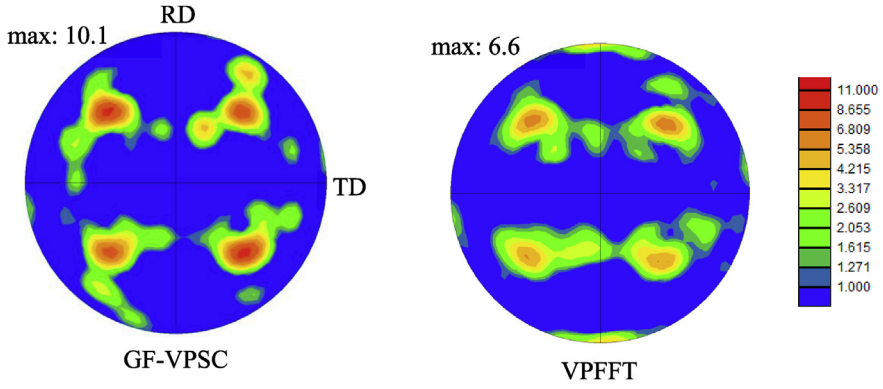

Fig. 11. {111} pole figures corresponding to transition band ODF for plane-strain compression of fcc polycrystal after 78% reduction predicted by GF-VPSC and VPFFT.

4. Conclusions

In this work, we have developed a formulation and the associated algorithms for the calculation of intragranular misorientation spreads during plastic deformation at high strains. The effect of the misorientation on the stress and lattice spin fluctuations has been included, by assuming linear relations between these fluctuations and misorientation. In addition, a grain fragmentation model, formulated in orientation space, was proposed and implemented in VPSC. The model was applied to tension of an fcc polycrystal and compared to the full-field simulation results obtained by VPFFT. It was observed that the dominant rotation axes tend to rotate toward the tensile direction, for grains that have reached stable [001] and [111] regions. This behavior was attributed to the effect of the lattice spin fluctuations caused by large intragranular misorientation spreads. In addition, PSC of fcc polycrystal at 400 °C to a strain of 1.2 was also simulated and compared with corresponding experiments and full-field simulations. It was observed that the dominant rotation axes at higher strains tend to align with RD. The magnitude of the spread evolves rapidly at lower strain and saturates at intermediate and high strains. The inclusion of misorientation spreads reduces the intensity of the deformed texture and

thus improves texture prediction. Considering the complexity of the physical problem, satisfactory agreement between the proposed model and full-field simulations and experiment was found. Finally, it was shown that the new GF-VPSC model can be used to predict microstructure evolution during deformation and recrystallization. Further development and applications of this novel modeling capability is on-going work, and will be reported in due time.

Acknowledgments

M.Z. and M.K acknowledge a subcontract, No. 388715, granted by Los Alamos National Laboratory (LANL) to the University of New Hampshire, and a project supported by the U.S. National Science Foundation under grant no. CMMI-1650641. R.A.L. acknowledges support from LANL's Laboratory-Directed Research and Development-Exploratory Research (LDRD-ER) project # 20180441ER.

Appendix A

The derivative of stress with respect to misorientation, $\delta\mathbf{r}$, can be obtained by taking the derivative of the rate-sensitive constitutive equation (Eq. (3)), holding the strain rate constant:

$$\frac{\partial\boldsymbol{\sigma}}{\partial\delta\mathbf{r}} = -\left[\sum_s \mathbf{m}^s \otimes \frac{\partial\dot{\gamma}^s}{\partial\boldsymbol{\sigma}}\right]^{-1}\left\{\sum_s\left[\mathbf{m}^s \otimes \left(\frac{\partial\dot{\gamma}^s}{\partial\mathbf{m}^s}\frac{\partial\mathbf{m}^s}{\partial\delta\mathbf{r}}\right) + \dot{\gamma}^s\frac{\partial\mathbf{m}^s}{\partial\delta\mathbf{r}}\right]\right\}. \tag{A1}$$

The derivatives of lattice reorientation rate (Eq. (13)) with respect to stress and misorientation are given by:

$$\frac{\partial\dot{\boldsymbol{\omega}}}{\partial\boldsymbol{\sigma}} = -\frac{\partial\dot{\boldsymbol{\omega}}^p}{\partial\boldsymbol{\sigma}} = -\sum_s \boldsymbol{\alpha}^s \otimes \frac{\partial\dot{\gamma}^s}{\partial\boldsymbol{\sigma}}, \tag{A2}$$

$$\frac{\partial\dot{\boldsymbol{\omega}}}{\partial\delta\mathbf{r}} = -\frac{\partial\dot{\boldsymbol{\omega}}^p}{\partial\delta\mathbf{r}} = -\sum_s\left[\boldsymbol{\alpha}^s \otimes \left(\frac{\partial\dot{\gamma}^s}{\partial\mathbf{m}^s}\frac{\partial\mathbf{m}^s}{\partial\delta\mathbf{r}}\right) + \dot{\gamma}^s\frac{\partial\boldsymbol{\alpha}^s}{\partial\delta\mathbf{r}}\right]. \tag{A3}$$

Note that the reorientation rate of ellipsoid is assumed to be constant in the grain. Consequently, derivatives of rotation rate are equal to the negative derivatives of the lattice spin given by Eq. (14).

Next, the expressions for derivatives $\frac{\partial\dot{\gamma}^s}{\partial\boldsymbol{\sigma}}$, $\frac{\partial\dot{\gamma}^s}{\partial\mathbf{m}^s}$, $\frac{\partial\mathbf{m}^s}{\partial\delta\mathbf{r}}$ and $\frac{\partial\boldsymbol{\alpha}^s}{\partial\delta\mathbf{r}}$ appearing in the 3 previous equations are provided. First, the derivatives of the shear rate (Eq. (2)) with respect to stress and the symmetric part of Schmid tensor are given by:

$$\frac{\partial\dot{\gamma}^s}{\partial\boldsymbol{\sigma}} = \dot{\gamma}_0 n\left(\frac{|\boldsymbol{\sigma}\colon\mathbf{m}^s|}{\tau_c^s}\right)^{n-1}\frac{1}{\tau_c^s}\mathbf{m}^s. \tag{A4}$$

$$\frac{\partial\dot{\gamma}^s}{\partial\mathbf{m}^s} = \dot{\gamma}_0 n\left(\frac{|\boldsymbol{\sigma}\colon\mathbf{m}^s|}{\tau_c^s}\right)^{n-1}\frac{1}{\tau_c^s}\boldsymbol{\sigma}. \tag{A5}$$

The derivative of symmetric Schmid tensors with respect to misorientation vector is given by the chain rule:

$$\frac{\partial m_{ij}^s}{\partial\delta r_m} = \frac{\partial m_{ij}^s}{\partial\delta R_{kl}}\frac{\partial\delta R_{kl}}{\partial\delta r_m}, \tag{A6}$$

where the δR_{kl} is rotation matrix representation of the rotation defined by the misorientation vector, δr_m. The derivative $\frac{\partial m_{ij}^s}{\partial\delta r_m}$ is evaluated at the mean orientation which implies zero misorientation. First, the derivative $\frac{\partial m_{ij}^s}{\partial\delta R_{kl}}$ evaluated at the mean orientation is:

$$\frac{\partial m_{ij}^s}{\partial\delta R_{kl}} = I_{ik} <m_{lj}^s> + I_{jk} <m_{il}^s>. \tag{A7}$$

In order to obtain the derivative $\frac{\partial\delta R_{ij}}{\partial\delta r_l}$, we write the misorientation matrix, δR_{ij}, as a function of misorientation vector, δr_k (Morawiec, 2004):

$$\delta R_{ij} = \begin{bmatrix} 1-2\delta r_2^2-2\delta r_3^2 & 2(\delta r_1\delta r_2 - \sqrt{1-\delta r_i\delta r_i}\,\delta r_3) & 2(\sqrt{1-\delta r_i\delta r_i}\,\delta r_2 + \delta r_1\delta r_3) \\ 2(\delta r_1\delta r_2 + \sqrt{1-\delta r_i\delta r_i}\,\delta r_3) & 1-2\delta r_1^2-2\delta r_3^2 & 2(\delta r_2\delta r_3 - \sqrt{1-\delta r_i\delta r_i}\,\delta r_1) \\ 2(\delta r_1\delta r_3 - \sqrt{1-\delta r_i\delta r_i}\,\delta r_2) & 2(\sqrt{1-\delta r_i\delta r_i}\,\delta r_1 + \delta r_2\delta r_3) & 1-2\delta r_1^2-2\delta r_2^2 \end{bmatrix} \tag{A8}$$

The derivatives of the misorientation matrix, δR_{ij}, with respect to misorientation vector, δr_k, evaluated at the mean orientation are:

$$\frac{\partial\delta R_{ij}}{\partial\delta r_1} = \begin{bmatrix} 0 & 0 & 0 \\ 0 & 0 & -2 \\ 0 & 2 & 0 \end{bmatrix};\ \frac{\partial\delta R_{ij}}{\partial\delta r_2} = \begin{bmatrix} 0 & 0 & 2 \\ 0 & 0 & 0 \\ -2 & 0 & 0 \end{bmatrix};\ \frac{\partial\delta R_{ij}}{\partial\delta r_3} = \begin{bmatrix} 0 & -2 & 0 \\ 2 & 0 & 0 \\ 0 & 0 & 0 \end{bmatrix}. \tag{A9}$$

The expressions for derivatives of the antisymmetric Schmid tensor are analogous to those of the symmetric Schmid tensor.

Appendix B

Let us consider two average intragranular stress fluctuation distributions at two subsequent time increments. The linear mapping of the stress fluctuation vectors at time $t - \Delta t$ to the corresponding statistical descriptor at time t, defined by matrix $\mathbf{Z}^{(r)}$, is needed. Let us assume both distributions are normal and perform a Cholesky decomposition of the stress fluctuations at times $t - \Delta t$ and t:

$$<\delta\boldsymbol{\sigma}^{t-\Delta t(\bar{q})} \otimes \delta\boldsymbol{\sigma}^{t-\Delta t(\bar{q})}>^{(r)} = \mathbf{L}^{t-\Delta t}(\mathbf{L}^{t-\Delta t})^T \tag{A10}$$

$$<\delta\boldsymbol{\sigma}^{t(\bar{q})} \otimes \delta\boldsymbol{\sigma}^{t(\bar{q})}>^{(r)} = \mathbf{L}^{t}(\mathbf{L}^{t})^T, \tag{A11}$$

where $\mathbf{L}^t$ and $\mathbf{L}^{t-\Delta t}$ are lower triangular matrices. The matrix $\mathbf{L}^t$ maps random five-dimensional vectors with zero mean and unit variance, to random vectors with zero mean and second moment defined by $<\delta\boldsymbol{\sigma}^{t(\bar{q})} \otimes \delta\boldsymbol{\sigma}^{t(\bar{q})}>^{(r)}$ (Press, 2007). Analogously, the matrix $\mathbf{L}^{t-\Delta t}$ performs similar mapping, but to random vectors with zero mean and second moment defined by $<\delta\boldsymbol{\sigma}^{t-\Delta t(\bar{q})} \otimes \delta\boldsymbol{\sigma}^{t-\Delta t(\bar{q})}>^{(r)}$. We can write the mapping $\mathbf{L}^t$ as composition of mapping $\mathbf{L}^{t-\Delta t}$ and mapping $\mathbf{Z}^{(r)}$:

$$\mathbf{L}^{t} = \mathbf{Z}^{(r)}\mathbf{L}^{t-\Delta t}. \tag{A12}$$

From here the matrix $\mathbf{Z}^{(r)}$ can be calculated as:

$$\mathbf{Z}^{(r)} = \mathbf{L}^{t}(\mathbf{L}^{t-\Delta t})^{-1}. \tag{A13}$$

Further, let us map the stress fluctuations $\delta\boldsymbol{\sigma}^{t-\Delta t(\bar{q})}(\mathbf{x})$ defined by the second moment $<\delta\boldsymbol{\sigma}^{t-\Delta t(\bar{q})} \otimes \delta\boldsymbol{\sigma}^{t-\Delta t(\bar{q})}>^{(r)}$ using matrix $\mathbf{Z}^{(r)}$ and show that the resulting distribution has second moment equal to $<\delta\boldsymbol{\sigma}^{t(\bar{q})} \otimes \delta\boldsymbol{\sigma}^{t(\bar{q})}>^{(r)}$:

$$\mathbf{Z}^{(r)} <\delta\boldsymbol{\sigma}^{t-\Delta t(\bar{q})} \otimes \delta\boldsymbol{\sigma}^{t-\Delta t(\bar{q})}>^{(r)} (\mathbf{Z}^{(r)})^T = \mathbf{L}^{t}\underbrace{(\mathbf{L}^{t-\Delta t})^{-1}\mathbf{L}^{t-\Delta t}}_{\mathbf{I}}\underbrace{(\mathbf{L}^{t-\Delta t})^T((\mathbf{L}^{t-\Delta t})^{-1})^T}_{\mathbf{I}}(\mathbf{L}^{t})^T = <\delta\boldsymbol{\sigma}^{t(\bar{q})} \otimes \delta\boldsymbol{\sigma}^{t(\bar{q})}>^{(r)}. \tag{A14}$$

$\mathbf{Z}^{(r)}$ represents the mapping of stress fluctuations from time $t - \Delta t$ to t when the cross-correlation between two stress fluctuations is perfect. However, in reality the cross-correlation is most likely very strong but not perfect. In the case of two correlated scalar variables, the proportionality between them is defined by the cross-correlation coefficient, ρ (Papoulis, 1991). We assume analogous relation for the multivariate case: $\mathbf{Z}^{(r)}(\rho) = \rho\mathbf{Z}^{(r)}(\rho = 1)$. The cross-correlation between five-dimensional stress fluctuations from two subsequent time increments is defined by the cross-correlation coefficient matrix but we approximate the strength of cross-correlation with only one scalar number ρ. We assume cross-correlation coefficient, ρ, is a function of strain increment given by:

$$\rho = 1.0 - 2.5 \times \Delta\varepsilon_{vm}. \tag{A15}$$

$\mathbf{Z}^{(r)}(\rho = 1)$ is linear mapping between stress fluctuation distributions when the cross-correlation is perfect (Eq. (A13) of the Appendix).

Appendix C

The three-dimensional parent's misorientation distribution described by the mean value, $\delta\mathbf{r}^{(r)} = 0$, and the second moment, $<\delta\mathbf{r} \otimes \delta\mathbf{r}>^{(r)}$, needs to be divided into two distributions, each described by its own mean value, $<\delta\mathbf{r}>^{(r)}_{f_i}$, and second moment, $<\delta\mathbf{r} \otimes \delta\mathbf{r}>^{(r)}_{f_i}$. First, we calculate the eigenvectors and eigenvalues of the parent's misorientation distribution and sort them in the descending order: $\mathbf{V} = [\mathbf{v}^1, \mathbf{v}^2, \mathbf{v}^3]$ and $\mathbf{E} = [\lambda^1, \lambda^2, \lambda^3]$. Next, we assume that the misorientation distribution is a multivariate normal distribution which implies that the distributions along the principal directions are normal and independent. Due to the independence of distributions along the different principal directions, the distribution along the direction of largest variation, $\mathbf{v}^1$, can be divided completely separately from the other two principal distributions. The three dimensional distributions of fragments are then created by combining the corresponding divided distributions along the direction of largest variation and the two other principal distributions.

The mean value of the left interval for one dimensional normal distribution is calculated as (Miller and Rice, 1983; Vazquez-Leal et al., 2012):

$$<x>^{left} = \frac{1}{F(0) - F(-\infty)}\int_{-\infty}^{0} xf(x)d\,\mathrm{x} = -2\sqrt{\frac{\lambda}{2\pi}}, \tag{A16}$$

where f and F denote probability density function and cumulative distribution function of normal distribution and λ is the variance. The variance of the left interval is calculated as (Miller and Rice, 1983; Vazquez-Leal et al., 2012):

$$<\delta x^2>^{left} = \frac{1}{F(0) - F(-\infty)}\int_{-\infty}^{0} x^2 f(x)d\,\mathrm{x} - (<x>^{left})^2 = \lambda\left(1 - \frac{2}{\pi}\right). \tag{A17}$$

The mean value and variance of the right interval are $<x>^{right} = -<x>^{left}$ and $<\delta x^2>^{right} = <\delta x^2>^{left}$. Using these expressions, the mean misorientations of the fragments with respect to the mean orientation of the parent are given by:

$$<\delta\mathbf{r}>^{(r)}_{f_1} = -2\sqrt{\frac{\lambda^1}{2\pi}}\mathbf{v}^1;\ <\delta\mathbf{r}>^{(r)}_{f_2} = 2\sqrt{\frac{\lambda^1}{2\pi}}\mathbf{v}^1. \tag{A18}$$

The mean orientations of fragments are then given by:

$$\bar{\mathbf{q}}_{f_1}^{(r)} = <\delta\mathbf{q}>_{f_1}^{(r)} \bar{\mathbf{q}}^{(r)};\ \bar{\mathbf{q}}_{f_2}^{(r)} = <\delta\mathbf{q}>_{f_2}^{(r)} \bar{\mathbf{q}}^{(r)}, \tag{A19}$$

where misorientations of fragments $<\delta\mathbf{q}>_{f_1}^{(r)}$ and $<\delta\mathbf{q}>_{f_2}^{(r)}$ are given by:

$$<\delta\mathbf{q}>_{f_1}^{(r)} = \begin{Bmatrix} \sqrt{1 - <\delta\mathbf{r}>_{f_1}^{(r)} \cdot <\delta\mathbf{r}>_{f_1}^{(r)}} \\ <\delta\mathbf{r}>_{f_1}^{(r)} \end{Bmatrix};\ <\delta\mathbf{q}>_{f_2}^{(r)} = \begin{Bmatrix} \sqrt{1 - <\delta\mathbf{r}>_{f_2}^{(r)} \cdot <\delta\mathbf{r}>_{f_2}^{(r)}} \\ <\delta\mathbf{r}>_{f_2}^{(r)} \end{Bmatrix}. \tag{A20}$$

The centered second moments of the fragments in the principal frame of the parent's distribution are:

$$<\delta\mathbf{r} \otimes \delta\mathbf{r}>_{f_1}^{(r),p} = <\delta\mathbf{r} \otimes \delta\mathbf{r}>_{f_2}^{(r),p} = \begin{bmatrix} \lambda^1\left(1 - \frac{2}{\pi}\right) & 0 & 0 \\ 0 & \lambda^2 & 0 \\ 0 & 0 & \lambda^3 \end{bmatrix}. \tag{A21}$$

The centered second moments of the fragments in sample frame are then obtained by simple coordinate transformation:

$$<\delta\mathbf{r} \otimes \delta\mathbf{r}>_{f_1}^{(r)} = <\delta\mathbf{r} \otimes \delta\mathbf{r}>_{f_2}^{(r)} = \mathbf{V} <\delta\mathbf{r} \otimes \delta\mathbf{r}>_{f_1}^{(r),p} \mathbf{V}^T. \tag{A22}$$

References

Ang, A.H.S., Tang, W.H., 1975. Probability Concepts in Engineering Planning and Design, Basic Principles. Wiley.

Ardeljan, M., Beyerlein, I.J., Knezevic, M., 2017. Effect of dislocation density-twin interactions on twin growth in AZ31 as revealed by explicit crystal plasticity finite element modeling. Int. J. Plast. 99, 81–101.

Ardeljan, M., Beyerlein, I.J., McWilliams, B.A., Knezevic, M., 2016. Strain rate and temperature sensitive multi-level crystal plasticity model for large plastic deformation behavior: application to AZ31 magnesium alloy. Int. J. Plast. 83, 90–109.

Ardeljan, M., Knezevic, M., Nizolek, T., Beyerlein, I.J., Mara, N.A., Pollock, T.M., 2015. A study of microstructure-driven strain localizations in two-phase polycrystalline HCP/BCC composites using a multi-scale model. Int. J. Plast. 74, 35–57.

Bachmann, F., Hielscher, R., Jupp, P.E., Pantleon, W., Schaeben, H., Wegert, E., 2010. Inferential statistics of electron backscatter diffraction data from within individual crystalline grains. J. Appl. Crystallogr. 43, 1338–1355.

Bacroix, B., Jonas, J., 1988. The influence of non-octahedral slip on texture development in fcc metals. Texture, Stress, Microstruct. 8, 267–311.

Beyerlein, I.J., Lebensohn, R.A., Tomé, C.N., 2003. Modeling texture and microstructural evolution in the equal channel angular extrusion process. Mater. Sci. Eng., A 345, 122–138.

Bobeth, M., Diener, G., 1986. Field fluctuations in multicomponent mixtures. J. Mech. Phys. Solid. 34, 1–17.

Buchheit, T.E., Carroll, J.D., Clark, B.G., Boyce, B.L., 2015. Evaluating deformation-induced grain orientation change in a polycrystal during in situ tensile deformation using EBSD. Microsc. Microanal. 21, 969–984.

Butler, G.C., McDowell, D.L., 1998. Polycrystal constraint and grain subdivision. Int. J. Plast. 14, 703–717.

Castañeda, P.P., 2002. Second-order homogenization estimates for nonlinear composites incorporating field fluctuations: I—theory. J. Mech. Phys. Solid. 50, 737–757.

Dillamore, I., Katoh, H., 1974. Mechanisms of recrystallization in cubic metals with particular reference to their orientation-dependence. Met. Sci. 8, 73–83.

Doghri, I., Brassart, L., Adam, L., Gérard, J.-S., 2011. A second-moment incremental formulation for the mean-field homogenization of elasto-plastic composites. Int. J. Plast. 27, 352–371.

Eshelby, J.D., 1957. The determination of the elastic field of an ellipsoidal inclusion, and related problems. Proc. Roy. Soc. Lond. A 241, 376–396.

Hansen, N., Jensen, D.J., 1999. Development of microstructure in FCC metals during cold work. Phil. Trans. Roy. Soc. Lond.: Mathematical, Physical and Engineering Sciences 357, 1447–1469.

Hjelen, J., Orsund, R., Nes, E., 1991. On the origin of recrystallization textures in aluminium. Acta Metall. Mater. 39, 1377–1404.

Humphreys, F., Hatherly, M., 2004. Recrystallization and Related Annealing Phenomena, 2004. Elsevier.

Jahedi, M., Ardeljan, M., Beyerlein, I.J., Paydar, M.H., Knezevic, M., 2015. Enhancement of orientation gradients during simple shear deformation by application of simple compression. J. Appl. Phys. 117, 214309.

Jahedi, M., Beyerlein, I.J., Paydar, M.H., Knezevic, M., 2018. Effect of grain shape on texture formation during severe plastic deformation of pure Copper Advanced engineering materials. 20, 1600829.

Jahedi, M., Beyerlein, I.J., Paydar, M.H., Zheng, S., Xiong, T., Knezevic, M., 2017. Effects of pressure and number of turns on microstructural homogeneity developed in high-pressure double torsion. Metall. Mater. Trans. 48, 1249–1263.

Jahedi, M., Paydar, M.H., Zheng, S., Beyerlein, I.J., Knezevic, M., 2014. Texture evolution and enhanced grain refinement under high-pressure-double-torsion. Mater. Sci. Eng., A 611, 29–36.

Kanjarla, A.K., Van Houtte, P., Delannay, L., 2010. Assessment of plastic heterogeneity in grain interaction models using crystal plasticity finite element method. Int. J. Plast. 26, 1220–1233.

Knezevic, M., Capolungo, L., Tomé, C.N., Lebensohn, R.A., Alexander, D.J., Mihaila, B., McCabe, R.J., 2012. Anisotropic stress-strain response and microstructure evolution of textured α-uranium. Acta Mater. 60, 702–715.

Knezevic, M., Crapps, J., Beyerlein, I.J., Coughlin, D.R., Clarke, K.D., McCabe, R.J., 2016. Anisotropic modeling of structural components using embedded crystal plasticity constructive laws within finite elements. Int. J. Mech. Sci. 105, 227–238.

Knezevic, M., Drach, B., Ardeljan, M., Beyerlein, I.J., 2014. Three dimensional predictions of grain scale plasticity and grain boundaries using crystal plasticity finite element models. Comput. Meth. Appl. Mech. Eng. 277, 239–259.

Knezevic, M., Kalidindi, S.R., Fullwood, D., 2008. Computationally efficient database and spectral interpolation for fully plastic Taylor-type crystal plasticity calculations of face-centered cubic polycrystals. Int. J. Plast. 24, 1264–1276.

Krog-Pedersen, S., Bowen, J.R., Pantleon, W., 2009. Quantitative characterization of the orientation spread within individual grains in copper after tensile deformation. Int. J. Mater. Res. 100, 433–438.

Kumar, M.A., Mahesh, S., 2013. Subdivision and microtexture development in fcc grains during plane strain compression. Int. J. Plast. 44, 95–110.

Lebensohn, R.A., 2001. N-site modeling of a 3D viscoplastic polycrystal using Fast Fourier Transform. Acta Mater. 49, 2723–2737.

Lebensohn, R.A., Brenner, R., Castelnau, O., Rollett, A.D., 2008. Orientation image-based micromechanical modelling of subgrain texture evolution in polycrystalline copper. Acta Mater. 56, 3914–3926.

Lebensohn, R.A., Liu, Y., Castaneda, P.P., 2004. On the accuracy of the self-consistent approximation for polycrystals: comparison with full-field numerical simulations. Acta Mater. 52, 5347–5361.

Lebensohn, R.A., Tomé, C.N., 1993. A self-consistent anisotropic approach for the simulation of plastic deformation and texture development of polycrystals: application to zirconium alloys. Acta Metall. Mater. 41, 2611–2624.
Lebensohn, R.A., Tomé, C.N., Castaneda, P.P., 2007. Self-consistent modelling of the mechanical behaviour of viscoplastic polycrystals incorporating intragranular field fluctuations. Phil. Mag. 87, 4287–4322.
Lebensohn, R.A., Zecevic, M., Knezevic, M., McCabe, R.J., 2016. Average intragranular misorientation trends in polycrystalline materials predicted by a viscoplastic self-consistent approach. Acta Mater. 104, 228–236.
Lee, C.S., Duggan, B.J., 1993. Deformation banding and copper-type rolling textures. Acta Metall. Mater. 41, 2691–2699.
Lequeu, P., Gilormini, P., Montheillet, F., Bacroix, B., Jonas, J.J., 1987. Yield surfaces for textured polycrystals .1. Crystallographic approach. Acta Metall. 35, 439–451.
Liu, Q., Jensen, D.J., Hansen, N., 1998. Effect of grain orientation on deformation structure in cold-rolled polycrystalline aluminium. Acta Mater. 46, 5819–5838.
Liu, Y., Castañeda, P.P., 2004. Second-order theory for the effective behavior and field fluctuations in viscoplastic polycrystals. J. Mech. Phys. Solid. 52, 467–495.
Masson, R., Bornert, M., Suquet, P., Zaoui, A., 2000. An affine formulation for the prediction of the effective properties of nonlinear composites and polycrystals. J. Mech. Phys. Solid. 48, 1203–1227.
McCabe, R.J., Richards, A.W., Coughlin, D.R., Clarke, K.D., Beyerlein, I.J., Knezevic, M., 2015. Microstructure effects on the recrystallization of low-symmetry alpha-uranium. J. Nucl. Mater. 465, 189–195.
Miller, A.C., Rice, T.R., 1983. Discrete approximations of probability-distributions. Manag. Sci. 29, 352–362.
Morawiec, A., 2004. Orientations and Rotations. Computations in Crystallographic Textures. Springer, Berlin.
Ostapovets, A., Šedá, P., Jäger, A., Lejček, P., 2012. New misorientation scheme for a visco-plastic self-consistent model: equal channel angular pressing of magnesium single crystals. Int. J. Plast. 29, 1–12.
Pantleon, W., 2005. Retrieving orientation correlations in deformation structures from orientation maps. Mater. Sci. Technol. 21, 1392–1396.
Pantleon, W., He, W., Johansson, T.P., Gundlach, C., 2008. Orientation inhomogeneities within individual grains in cold-rolled aluminium resolved by electron backscatter diffraction. Mater. Sci. Eng. A-Struct. Mater. Prop. Microstruct. Process 483–84, 668–671.
Papoulis, A., 1991. Probability, Random Variables and Stochastic Processes. McGraw-Hill, Inc., New York.
Perocheau, F., Driver, J., 2002. Slip system rheology of Al–1% Mn crystals deformed by hot plane strain compression. Int. J. Plast. 18, 185–202.
Press, W.H., 2007. Numerical Recipes 3rd Edition: the Art of Scientific Computing. Cambridge university press.
Quey, R., Dawson, P.R., Driver, J.H., 2012. Grain orientation fragmentation in hot-deformed aluminium: experiment and simulation. J. Mech. Phys. Solid. 60, 509–524.
Quey, R., Driver, J.H., Dawson, P.R., 2015. Intra-grain orientation distributions in hot-deformed aluminium: orientation dependence and relation to deformation mechanisms. J. Mech. Phys. Solid. 84, 506–527.
Quey, R., Piot, D., Driver, J., 2010. Microtexture tracking in hot-deformed polycrystalline aluminium: experimental results. Acta Mater. 58, 1629–1642.
Ridha, A., Hutchinson, W., 1982. Recrystallisation mechanisms and the origin of cube texture in copper. Acta Metall. 30, 1929–1939.
Tomé, C., Necker, C., Lebensohn, R., 2002. Mechanical anisotropy and grain interaction in recrystallized aluminum. Metall. Mater. Trans. 33, 2635–2648.
Toth, L.S., Estrin, Y., Lapovok, R., Gu, C.F., 2010. A model of grain fragmentation based on lattice curvature. Acta Mater. 58, 1782–1794.
Vazquez-Leal, H., Castaneda-Sheissa, R., Filobello-Nino, U., Sarmiento-Reyes, A., Sanchez Orea, J., 2012. High accurate simple approximation of normal distribution integral. Math. Probl Eng. 2012.
Winther, G., Wright, J.P., Schmidt, S., Oddershede, J., 2017. Grain interaction mechanisms leading to intragranular orientation spread in tensile deformed bulk grains of interstitial-free steel. Int. J. Plast. 88, 108–125.
Zecevic, M., Pantleon, W., Lebensohn, R.A., McCabe, R.J., Knezevic, M., 2017. Predicting intragranular misorientation distributions in polycrystalline metals using the viscoplastic self-consistent formulation. Acta Mater. 140, 398–410.